JNC TY9400 2002-014

Study on a Numerical Simulation for Thermal - Hydraulic Phenomena of Multiphase, Multicomponent Flows

- Modeling of Multiphase, Multicomponent Flows with Phase Transition -

May 2002

O-arai Engineering Center
Japan Nuclear Cycle Development Institute

Ⓝ

JNC TY9400 2002-014
May, 2 0 0 2

Study on a Numerical Simulation for Thermal-Hydraulic Phenomena of Multiphase, Multicomponent Flows

– Modeling for Multiphase, Multicomponent Flows with Phase Transition –

Koji MORITA*, Tatsuya MATSUMOTO*, Kenji FUKUDA*
Tohru SUZUKI**, Yoshiharu TOBITA**, Hidemasa YAMANO**, Satoru KONDO***

Abstract

It is one of important problems for more reliable safety evaluation to improve numerical simulation techniques for thermal-hydraulic phenomena of multiphase, multicomponent flows in a safety analysis code for core disruptive accidents. In collaboration with the Japan Nuclear Cycle Development Institute and Kyushu University, a new multicomponent vaporization/condensation (V/C) model was developed to provide a generalized model for a fast reactor safety analysis code, which analyzes accident sequences of core disruptive accidents (CDAs). The model characterizes the V/C process through heat-transfer and mass-diffusion limited models to simulate the multicomponent phase-transition phenomena under CDA conditions. The heat-transfer limited model describes the nonequilibrium phase-transition processes occurring at interfaces, while the mass-diffusion limited model is employed to represent effects of noncondensable gases and multicomponent mixture on V/C processes. By analyzing a newly performed multi-bubble condensation experiment as well as available condensation experiments, validation of the model and method employed was demonstrated successfully for the steam condensation behaviors with noncondensable gases.

Work performed under contracts between Kyushu University and Japan Nuclear Cycle Development Institute

* Institute of Environmental Systems, Graduate School of Engineering, Kyushu University
** Nuclear System Safety Research Group, Advanced Technology Division, O-arai Engineering Center
*** Advanced Technology Division, O-arai Engineering Center

JNC TY9400 2002-014
2002年5月

多成分多相流の熱流動現象の数値シミュレーションに関する研究
ー相変化を伴う多成分多相流のモデル化手法の開発ー

（先行基礎工学研究に関する平成13年度共同研究報告書）

守田 幸路*, 松元 達也*, 福田 研二*
鈴木 徹**, 飛田 吉春**, 山野 秀将**, 近藤 悟***

要　旨

炉心損傷事故の安全解析コードにおける多成分多相流の熱流動現象の数値シミュレーション技術の高度化を図ることは，安全評価の信頼度を向上する上で重要な課題の一つである。核燃料サイクル開発機構と九州大学によって実施された本共同研究では，炉心損傷事故（CDA）を解析する高速炉安全解析コードに適用可能な多成分系蒸発／凝縮現象の一般化モデルを新たに開発した。このモデルは，CDA 条件下での多成分相変化現象を模擬するため，蒸発／凝縮過程の特性を熱伝達および質量拡散による律速モデルを用いて記述している。さらに，既存の多成分凝縮実験および新たに実施した気泡群凝縮実験の解析によって，本モデルが非凝縮性ガスを含む蒸気の凝縮過程を適切に再現することを確認し，用いられたモデル化手法の妥当性を示した。

本研究は，先行基礎工学研究に関する研究協力として，九州大学と核燃料サイクル開発機構との共同研究として実施したものである。

*　九州大学大学院工学研究院 附属環境システム科学研究センター

**　大洗工学センター，要素技術開発部，リスク評価研究グループ

***　大洗工学センター，要素技術開発部

List of contents

List of figures

1. Introduction

The consequences of postulated core disruptive accidents (CDAs) have been a major concern in the safety of liquid-metal fast reactors (LMFRs), because of the energetics potential resulting from a recriticality event. Mechanistic simulation of an accident sequence during a CDA is required to realistically assess the energetics potential. This is only achieved by using a comprehensive computational tool that systematically models multiphase thermohydraulic and neutronic phenomena occurring during the so-called transition and expansion phases of a CDA. In this area, the SIMMER-II code was developed as the first practical tool of its kind [1], and has been used in many experimental and reactor analyses [2]. The code has played a pioneering role especially in advancement of the mechanistic simulation of CDAs, but at the same time extensive worldwide code application revealed many limitations due to the code framework as well as needs for model improvement. For this reason, the development of a new code, SIMMER-III, has been conducted at the Japan Nuclear Cycle Development Institute (JNC) [3] initially in collaboration with the Los Alamos National Laboratory, the United States, and more recently with Forschungszentrum Karlsruhe (FZK), Germany, and Commissariat à l'Energie Atomique (CEA), France. The development of SIMMER-III has reached a stage, where all the models originally intended are made available and integral calculations with the code can be made [4]. In parallel to the code development, an extensive program has been performed for systematic and comprehensive code assessment under the collaboration with FZK and CEA [5, 6]. Furthermore, some reactor applications have been performed successfully [7, 8]. Although the original objective of SIMMER-III was primarily to resolve some of the key LMFR CDA issues, its flexible framework enables us to apply the code to various areas of interest, which are consistent with the modeling framework. Therefore, the code application could include: accident analyses of any types of future or advanced liquid-metal cooled reactors [9], steam-explosion problems in current- and future-generation light water reactors [10], and general types of multiphase flow problems.

The multicomponent vaporization/condensation (V/C) model is one of the key constitutive models of SIMMER-III to simulate heat- and mass-transfer phenomena relevant to accident sequences of CDAs. The objective of the present study is to develop a V/C model that reliably describes the multicomponent phase-transition process for core materials in sufficient physical details for use in LMFR accident analysis. The development is intended to provide a generalized model that is useful for analyzing relatively short-time-scale multiphase, multicomponent hydraulic problems, among which vaporization and condensation, or simultaneous heat and mass transfer, play an important role. The model characterizes the V/C process associated with phase transition through heat-transfer and mass-diffusion limited models to follow the time evolution of the rector core under CDA conditions. The outcome and experience gained in course of the SIMMER-II and AFDM developments [1, 11] were used to maximum extent. This paper is the first in a series of two papers reporting the development of multicomponent V/C model for SIMMER-III. Here, the model and method employed in the multicomponent V/C model are described, and then its basic validity is demonstrated using two series of multicomponent phase-transition experiments. The model applicability to the reactor safety analysis will be also discussed with results of PDE (post-disassembly expansion) analysis for a fast reactor.

2. Outline of SIMMER-III multiphase models

SIMMER-III is a two-dimensional, three-velocity-field, multiphase, multicomponent, Eulerian, fluid-dynamics code coupled with a fuel-pin model and a space- and energy-dependent neutron kinetics model [6]. The code models five basic LMFR core materials: mixed-oxide fuel, stainless steel, sodium, control (B_4C) and fission gas. A material can exist as different physical states, for example fuel needs to be represented by fabricated pin fuel, liquid fuel, a crust refrozen on structure, solid particles and fuel vapor, although fission gas exists only in the gaseous state. The material mass distributions are modeled by 27 density components, while the energy distributions are modeled by only 16 energy components since some density components are assigned to the same energy component. The structure field components, which consist of fuel pins and can walls, are immobile. Three velocity fields (two for liquids and one for vapor) are modeled to simulate relative fluid motions adequately, such as fuel/steel separation in a molten core pool and inter-penetration of fuel into sodium. Each mobile component, which is liquid, solid particle or vapor, is assigned to one of three velocity fields. Although SIMMER-III is tailored to LMFR materials, the code is sufficiently flexible to model non-LMFR materials, which are present in many assessment problems and advanced reactors.

The overall fluid-dynamics solution algorithm is based on a time-factorization (time-splitting) approach developed for AFDM [12], in which intra-cell interfacial area source terms, momentum exchange functions and heat and mass transfer are determined separately from inter-cell fluid convection. A semi-implicit procedure is used to solve inter-cell convection on an Eulerian staggered mesh and a higher-order differencing scheme is implemented to improve the resolution of fluid interfaces by minimizing numerical diffusion. A simultaneous solution of all the conservation equations would be complex and inefficient numerically, and hence this solution procedure of separating intra-cell transfers from fluid convection is believed to be the most practical for complex multicomponent systems such as SIMMER-III.

In SIMMER-III, there are 42 contact interfaces among seven fluid energy components (liquid fuel, steel, sodium; fuel, steel and control particles; and vapor mixture) and three structure surfaces (a fuel pin and two can walls). The constitutive models describe intra-cell transfer of mass, momentum and energy at the fluid interfaces. SIMMER-III also has a model for convective interfacial areas to take better account of highly transient flow [13]. The calculations of intra-cell heat and mass transfer include: structure configuration and heat and mass transfer due to structure breakup, multiple flow regime treatment and interfacial areas with source terms, momentum exchange functions for each flow regime, inter-cell heat transfer due to conduction, melting and freezing, vaporization and condensation, etc.

In addition to the constitutive models, an equation-of-state (EOS) model is required to close and complete the fluid-dynamic conservation equations. The analytic EOS model in SIMMER-III employs flexible thermodynamic functions [14, 15], which treat the basic reactor-core materials. These materials are assumed to be immiscible, such that a unique EOS for each material can be defined. The structure model represents the configuration and time-dependent disintegration of the fuel pins and subassembly can walls. Two can walls can be modeled at the left and right mesh cell boundaries, each of which contains two temperature nodes. The presence of a can wall at a cell boundary prevents radial fluid convection, and provides a surface where fuel can freeze or vapor can condense.

3. Model and method in V/C calculation

3.1. Nonequilibrium mass-transfer model

In SIMMER-III, the phase-transition processes occurring at interfaces are described with a heat-transfer limited model. These are nonequilibrium processes because the bulk temperature does not generally satisfy the phase-transition condition when the mass transfer occurs at the interface. The basic concept of this model is illustrated in Fig. 1, where a binary contact interface of the energy components A and B is shown. Each energy component interfaces with the other energy components simultaneously, and each interface has a uniquely defined interfacial area. Energy transfers between components are based on the interfacial area and heat-transfer coefficients determined from engineering correlations. A specified temperature is assigned to each possible interface to calculate heat flows from/to each interface into/from the respective bulk materials. These heat flows are summed to give net interfacial energy loss or gain. The net energy transfer rate from the interface is defined as

$$q^{\mathrm{I}}_{\mathrm{A,B}} = a_{\mathrm{A,B}}\left[h_{\mathrm{A,B}}(T^{\mathrm{I}}_{\mathrm{A,B}} - T_{\mathrm{A}}) + h_{\mathrm{B,A}}(T^{\mathrm{I}}_{\mathrm{A,B}} - T_{\mathrm{B}})\right] \tag{1}$$

An interfacial energy loss is defined as positive and means condensation must occur to conserve (provide) energy. An interfacial energy gain, which is defined as negative, means the energy is going into vaporization. For example, Fig. 1 shows interface (A, B) where the interface is undergoing a net loss energy to component B. This energy is either coming from condensation of component A. The resulting product will be either more of component B, or component C depending on the process involved. When the phase transition is predicted, the interface temperature $T^{\mathrm{I}}_{\mathrm{A,B}}$ is defined as the bulk saturation temperature of a phase-transition species. Otherwise, in the case of no mass transfer, the interface energy transfer is zero and hence the equivalent interface temperature should be

$$T^{\mathrm{I}}_{\mathrm{A,B}} = \frac{h_{\mathrm{A,B}}T_{\mathrm{A}} + h_{\mathrm{B,A}}T_{\mathrm{B}}}{h_{\mathrm{A,B}} + h_{\mathrm{B,A}}} \tag{2}$$

The phase-transition rate is determined from energy balance at the interface. If the net heat flow $q^{\mathrm{I}}_{\mathrm{A,B}}$ is zero, sensible heat is exchanged without phase transition. If $q^{\mathrm{I}}_{\mathrm{A,B}}$ is positive, namely the energy is lost at the interface, a vapor component condenses. Then the mass-transfer rate for this case is determined from:

if the component formed by the phase transition is B,

$$\Gamma^{\mathrm{I}}_{\mathrm{A,B}} = R_{\mathrm{A,B}} \frac{q^{\mathrm{I}}_{\mathrm{A,B}}}{i_{\mathrm{A}} - i^{\mathrm{I}}_{\mathrm{B}}}, \text{ or} \tag{3}$$

if component C formed by the phase transition is not B,

$$\Gamma^{\mathrm{I}}_{\mathrm{A,C}} = R_{\mathrm{A,B}} \frac{q^{\mathrm{I}}_{\mathrm{A,B}}}{i_{\mathrm{A}} - i^{\mathrm{I}}_{\mathrm{C}}} \tag{4}$$

If $q^{\mathrm{I}}_{\mathrm{A,B}}$ is negative, on the other hand, namely the energy is gained at the interface, a liquid component vaporizes. Then the mass-transfer rate for this case is determined from:

if the component formed by the phase transition is A,

$$\Gamma^{\mathrm{I}}_{\mathrm{B,A}} = -R_{\mathrm{A,B}} \frac{q^{\mathrm{I}}_{\mathrm{A,B}}}{i^{\mathrm{I}}_{\mathrm{A}} - i_{\mathrm{B}}}, \text{ or} \tag{5}$$

if component D formed by the phase transition is not A,

$$\Gamma^{\mathrm{I}}_{\mathrm{B,D}} = -R_{\mathrm{A,B}} \frac{q^{\mathrm{I}}_{\mathrm{A,B}}}{i^{\mathrm{I}}_{\mathrm{D}} - i_{\mathrm{B}}} \tag{6}$$

The right sides of the above four equations are multiplied by a correction factor $R_{\mathrm{A,B}}$, which is introduced to take account of the effect of noncondensable gases and multicomponent mixtures on vaporization and condensation at the vapor/liquid and vapor/solid interfaces. Typically, the condensation rate can be reduced significantly when noncondensable gases are present in the vapor mixture due to a buildup of noncondensable-gas concentration at which condensation occurs, reducing the condensation saturation temperature below the bulk mixture saturation temperature. The procedure to determine $R_{\mathrm{A,B}}$ based on the mass-diffusion limited processes is discussed in the next section. It should be also noted that the latent heat of phase transition is defined here as the difference between the enthalpy at the interface and the bulk enthalpy of a component undergoing a phase-transition process. Although more correctly the bulk enthalpy should be replaced by the interfacial one, SIMMER-III does not calculate temperature gradients in liquid and vapors. Besides, the experience from the previous codes suggests that better results are obtained with this definition of effective latent heat [11, 16].

3.2. Effect of multicomponent mixture

The physical model to represent the effect of noncondensable gases and multicomponent mixtures on V/C processes is based on a study originally attempted for SIMMER-II [1]. The equations for this model were obtained by considering the quasi-steady, stagnant Couette-flow boundary layer, as shown Fig. 2, to relate the mass and energy fluxes to the overall forces driving heat and mass. This classical Couette-flow model has been shown to provide a good engineering model for single-component vapor condensation in the presence of noncondensable gases, thus confirming the adequacy of its theory for incorporation in two-fluid computer codes [17, 18, 19]. In SIMMER-II, the model extended to multicomponent systems was designed to predict not only the suppression of condensation by noncondensable gases such as a fission gas, but also the phase-transition rate for a vapor component condensing on the surface of a different material. However, this previous effort was not successful for the practical use of the code because its solution scheme was incompatible with numerical algorithms applied to SIMMER-II multiphase-flow modeling. In the present study, extensive model modifications are made as necessary and a new solution scheme is developed to make it suitable for implementation on the multi-fluid computer code, SIMMER-III.

The physical model and coordinate system are shown in Fig. 2. A multicomponent vapor mixture at temperature T_{g} and mass fraction $\omega_{\mathrm{k},\infty}$ (k = 1...N) is under the phase transition on a liquid or solid phase, which is maintained at a constant temperature T_{0}. Here, the conservation of each vapor species can be described based on multicomponent diffusion law given, for example, by Bird et al. [20]. Assuming that mass diffusion due to thermal and pressure gradient is negligibly small, the mass-transfer rate of vapor component k at the interface i, defined positive for condensation, is governed by

$$\Gamma_{\mathrm{k}} = a_{\mathrm{i}} \rho_{\mathrm{g}} D_{\mathrm{kg}} \left. \frac{d\omega_{\mathrm{k}}}{dy} \right|_{\mathrm{i}} + \omega_{\mathrm{k,i}} \sum_{\mathrm{j=1}}^{\mathrm{N}} \Gamma_{\mathrm{j}} \qquad (7)$$

This equation includes both diffusive and convective contribution.

The heat flow per unit volume at the interface should include contribution of heat conduction, bulk convection and diffusion, that is

$$q_{\mathrm{i}} = -a_{\mathrm{i}}\kappa\left.\frac{dT}{dy}\right|_{\mathrm{i}} - \sum_{\mathrm{j}=1}^{\mathrm{N}}\Gamma_{\mathrm{j}}i_{\mathrm{j}} \tag{8}$$

Thus, approximating the temperature gradients by overall heat-transfer coefficients, energy balance applied to the interface yields

$$a_{\mathrm{i}}h_{\mathrm{g}}^{*}(T_{\mathrm{i}} - T_{\mathrm{g}}) - \sum_{\mathrm{j}=1}^{\mathrm{N}}\Gamma_{\mathrm{j}}i_{\mathrm{j,g}} = -a_{\mathrm{i}}h_{\mathrm{o}}(T_{\mathrm{i}} - T_{\mathrm{o}}) - \sum_{\mathrm{j}=1}^{\mathrm{N}}\Gamma_{\mathrm{j}}i_{\mathrm{j,o}} \tag{9}$$

where h_{g}^{*} is the vapor-side heat-transfer coefficient in the presence of mass transfer, and hence the effect of mass flow through the boundary layer can be accounted for by [20]

$$h_{\mathrm{g}}^{*} = -\frac{\sum_{\mathrm{j}=1}^{\mathrm{N}}\Gamma_{\mathrm{j}}c_{\mathrm{p,j}}\Big/a_{\mathrm{i}}}{\exp\left(-\sum_{\mathrm{j}=1}^{\mathrm{N}}\Gamma_{\mathrm{j}}c_{\mathrm{p,j}}\Big/a_{\mathrm{i}}h_{\mathrm{g}}\right) - 1} \tag{10}$$

Eq. (9) represents that the heat flow at the interface equals the sum of the latent heat flow and the sensible heat flow through the interface.

The second term on the right side of Eq. (7) is simplified by introducing the mass-transfer coefficient in a manner analogous to the heat-transfer coefficients, that is

$$\rho_{\mathrm{g}}D_{\mathrm{kg}}\left.\frac{d\omega_{\mathrm{k}}}{dy}\right|_{\mathrm{i}} = -k_{\mathrm{k}}^{*}(\omega_{\mathrm{k.i}} - \omega_{\mathrm{k},\infty}) \tag{11}$$

where the mass-transfer coefficient k_{k}^{*} in the presence of mass transfer is also modeled by [20]

$$k_{\mathrm{k}}^{*} = -\frac{\sum_{\mathrm{j}=1}^{\mathrm{N}}\Gamma_{\mathrm{j}}\Big/a_{\mathrm{i}}}{\exp\left(-\sum_{\mathrm{j}=1}^{\mathrm{N}}\Gamma_{\mathrm{j}}\Big/a_{\mathrm{i}}k_{\mathrm{k}}\right) - 1} \tag{12}$$

The mass fraction $\omega_{\mathrm{k.i}}$ of the vapor component k at the interface is determined by the relation between mass and mole fractions:

$$\omega_{\mathrm{k.i}} = \frac{x_{\mathrm{k.i}}W_{\mathrm{k}}}{\sum_{\mathrm{j}=1}^{\mathrm{N}}x_{\mathrm{j,i}}W_{\mathrm{j}} + \left(1 - \sum_{\mathrm{j}=1}^{\mathrm{N}}x_{\mathrm{j,i}}\right)W_{\mathrm{ng}}} \tag{13}$$

The mole fractions of vapor component at the interface are obtained by assuming a constant pressure through the boundary layer to the interface. In addition, the condensed phase at the interface is assumed to be in saturated thermodynamic equilibrium with the vapor component, of which saturation pressure in the immiscible system is independent of its concentration in the condensed phase. Treating the vapor components and noncondensable gases as a mixture of ideal gases, the mole fraction $x_{\mathrm{k,i}}$ of vapor component k at the interface is related to the interface temperature T_{i} according to

$$x_{\mathrm{k,i}} = \frac{p_{\mathrm{sat.k}}(T_{\mathrm{i}})}{p_{\mathrm{g}}} \tag{14}$$

where $p_{\mathrm{sat.k}}(T_{\mathrm{i}})$ is the saturation pressure of a phase-transition component at the interface and p_{g} is the total pressure. The total pressure p_{g} is expressed as the sum of $p_{\mathrm{sat.k}}(T_{\mathrm{i}})$ and the partial pressure of the noncondensable gases at the interface:

$$p_{\mathrm{g}} = \sum_{\mathrm{j=1}}^{\mathrm{N}} p_{\mathrm{sat.j}}(T_{\mathrm{i}}) + p_{\mathrm{ng,i}} \tag{15}$$

In summary, the interface equations of the mass-diffusion limited model to be solved are described by

$$\Gamma_{\mathrm{k}} = -a_{\mathrm{i}} k_{\mathrm{k}}^{*} (\omega_{\mathrm{k,i}} - \omega_{\mathrm{k},\infty}) + \omega_{\mathrm{k,i}} \sum_{\mathrm{j=1}}^{\mathrm{N}} \Gamma_{\mathrm{j}},\ \mathrm{k} = 1 \ldots \mathrm{N} \tag{16}$$

$$\sum_{\mathrm{j=1}}^{\mathrm{N}} \Gamma_{\mathrm{j}} i_{\mathrm{lg.j}} = a_{\mathrm{i}} \left[h_{\mathrm{g}}^{*} (T_{\mathrm{i}} - T_{\mathrm{g}}) + h_{\mathrm{o}} (T_{\mathrm{i}} - T_{\mathrm{o}}) \right] \tag{17}$$

where i_{lg} is the latent heat of vaporization as the enthalpy difference between i_{g} and i_{o}, but is replaced with the effective latent heat as already discussed. In the presence of noncondensable gases, a simultaneous solution of Eqs. (16) and (17) in terms of the interface temperature T_{i} can be obtained iteratively although there is nonlinear thermodynamic relationships between T_{i} and the partial pressures of vapor components. For the case of no noncondensable gas, T_{i} is evaluated as an iterative solution of Eq. (15) with $p_{\mathrm{ng,i}} = 0$:

$$\sum_{\mathrm{j=1}}^{\mathrm{N}} p_{\mathrm{sat.j}}(T_{\mathrm{i}}) = p_{\mathrm{g}} \tag{18}$$

As mentioned in the previous section, the correction factor R is introduced into the heat-transfer limited model to represent the mass-diffusion limited behaviors for each mass-transfer rate at the vapor/liquid and valor/solid interfaces. To recast both heat-transfer and mass-diffusion limited processes in a mathematical form compatible with a V/C numerical solution algorithm described in the next chapter, R_k for the component k undergoing a phase transition is defined as a correction for the mass-transfer rate of pure vapor:

$$R_k = \frac{\Gamma_k(T_i)}{\Gamma_k(T_{sat,k})} \tag{19}$$

where

$$\Gamma_k(T_i) = \frac{a_i\left[h_g^*(T_i - T_g) + h_o(T_i - T_o)\right]}{i_{lg,k}} \text{ and} \tag{20}$$

$$\Gamma_k(T_{sat,k}) = \frac{a_i\left[h_g(T_{sat,k} - T_g) + h_o(T_{sat,k} - T_o)\right]}{i_{lg,k}} \tag{21}$$

The mass-transfer rate $\Gamma_k(T_i)$ is defined as a function of T_i, which is a solution of Eqs. (16) and (17) or Eq. (18), while $\Gamma_k(T_{sat,k})$ is the mass-transfer rate obtained assuming that the interface temperature is equal to the bulk saturation temperature $T_{sat,k}(p_k)$ and the vapor-side heat-transfer coefficient is independent of mass transfer. The correction factor R_k can be evaluated independently prior to the implicit calculation of V/C conservation equations, even though the iterative solution of several coupled nonlinear equations to evaluate the interface temperature is required at each vapor interface. Thus, it is unnecessary for us to employ a numerical scheme to obtain a simultaneous solution of the interface temperature and V/C conservation equations. This is advantageous because such a scheme would be complex and inefficient numerically.

3.3. Mass-transfer paths

In SIMMER-III, the seven fluid energy components have 21 binary contact modes, and each fluid component can interact with the three structures. Fig. 3 illustrates typical mass-transfer paths among a vapor mixture and three liquid components. The liquid vaporization can occur at the liquid/liquid interfaces as well as at the vapor/liquid interfaces. Condensation processes of fuel or steel vapor on other colder liquids can be considered at the vapor/liquid interfaces. The vapor condensation on solid particles and structures are also treated in the V/C transfers. As the results, in SIMMER-III 30 paths are treated as the nonequilibrium V/C processes occurring at interfaces, which have major effects on key phenomena directly relevant to accident sequences of a CDA. The phenomena include boiling pool dynamics, material expansion (through a channel and into a pool), fuel-coolant interactions and so on. Total V/C mass-transfer rates involving all the V/C paths are presented as follows:

$$\Gamma_{G,L1} = \Gamma_{G,L1}^{I(G/L1)} + \Gamma_{G,L1}^{I(G/L2)} + \Gamma_{G,L1}^{I(G/L3)} + \sum_{k=1}^{6} \Gamma_{G,L1}^{I(G/K(k))} \tag{22}$$

$$\Gamma_{G,L2} = \Gamma_{G,L2}^{I(G/L2)} + \Gamma_{G,L2}^{I(G/L3)} + \sum_{k=1}^{6} \Gamma_{G,L2}^{I(G/K(k))} \tag{23}$$

$$\Gamma_{G,L3} = \Gamma_{G,L3}^{I(G/L3)} + \sum_{k=1}^{6} \Gamma_{G,L3}^{I(G/K(k))} \tag{24}$$

$$\Gamma_{L1,G} = \Gamma_{L1,G}^{I(G/L1)} \tag{25}$$

$$\Gamma_{L2,G} = \Gamma_{L2,G}^{I(G/L2)} + \Gamma_{L2,G}^{I(L1/L2)} \text{ and} \tag{26}$$

$$\Gamma_{L3,G} = \Gamma_{L3,G}^{I(G/L3)} + \Gamma_{L3,G}^{I(L1/L3)} + \Gamma_{L3,G}^{I(L2/L3)} \tag{27}$$

Here, detailed expressions of the typical V/C mass-transfer rates are described for vapor/liquid-sodium, vapor/solid and liquid-fuel/liquid-sodium interfaces.

At the interface between vapor and liquid sodium, fuel and steel vapor can condense on liquid sodium and sodium can either condense or vaporize. The interfacial energy transfer rates are evaluated by

$$q_{Gm,L3}^{I} = a_{G,L3}[h_{L3,G}(T_{Gm,L3}^{I} - T_{Lm}) + h_{G,L3}(T_{Gm,L3}^{I} - T_{G})], \text{ m} = 1, 2 \text{ and } 3 \tag{28}$$

The interface temperatures are expressed by

$$T_{Gm,L3}^{I} = \max[T_{Sat,Gm}, T_{GL3}], \text{ m} = 1 \text{ and } 2, \text{ and} \tag{29}$$

$$T_{G3,L3}^{I} = T_{Sat,G3} \tag{30}$$

where the interface temperature T_{GL3} in the case of no mass transfer is given by

$$T_{GL3} = \frac{h_{L3,G}T_{L3} + h_{G,L3}T_{G}}{h_{L3,G} + h_{G,L3}} \tag{31}$$

The mass-transfer rates at this interface are expressed by

$$\Gamma_{\mathrm{G,Lm}}^{\mathrm{I(G/L3)}} = R_{\mathrm{Gm,L3}} \frac{q_{\mathrm{Gm,L3}}^{\mathrm{I}}}{i_{\mathrm{Gm}} - i_{\mathrm{Con,Gm}}},\ q_{\mathrm{Gm,L3}}^{\mathrm{I}} > 0 \text{ and} \tag{32}$$

$$\Gamma_{\mathrm{L3,G}}^{\mathrm{I(G/L3)}} = -R_{\mathrm{G3,L3}} \frac{q_{\mathrm{G3,L3}}^{\mathrm{I}}}{i_{\mathrm{Vap,G3}} - i_{\mathrm{L3}}},\ q_{\mathrm{G3,L3}}^{\mathrm{I}} < 0 \tag{33}$$

Eq. (32) for m = 1, 2 and 3 is used for fuel, steel and sodium condensation, respectively, and Eq. (33) is used for sodium vaporization. Similar treatment is applied to vapor/liquid-fuel interface, where fuel can either condense or vaporize; vapor/liquid-steel interface, where fuel vapor can condense on liquid steel and steel can either condense or vaporize.

At the interfaces between vapor and solid components such as particles and structures, fuel, steel and sodium vapor can condense on their surfaces. The interfacial energy transfer rates are evaluated by

$$q_{\mathrm{Gm,K(k)}}^{\mathrm{I}} = a_{\mathrm{G,K(k)}}[h_{\mathrm{K(k)}}(T_{\mathrm{Gm,K(k)}}^{\mathrm{I}} - T_{\mathrm{K(k)}}) + h_{\mathrm{G,K(k)}}(T_{\mathrm{Gm,K(k)}}^{\mathrm{I}} - T_{\mathrm{G}})],\ \mathrm{m} = 1, 2 \text{ and } 3 \tag{34}$$

where K(k) for k = 1 – 6 represents L4, L5 and L6 for particles, and k1, k2 and k3 for structure surfaces, respectively. The interface temperatures are expressed by

$$T_{\mathrm{Gm,K(k)}}^{\mathrm{I}} = \max[T_{\mathrm{Sat,Gm}}, T_{\mathrm{GK(k)}}],\ \mathrm{m} = 1, 2 \text{ and } 3 \tag{35}$$

where the interface temperatures $T_{\mathrm{GK(k)}}$ in the case of no mass transfer is given by

$$T_{\mathrm{GK(k)}} = \frac{h_{\mathrm{K(k)}} T_{\mathrm{K(k)}} + h_{\mathrm{G,K(k)}} T_{\mathrm{G}}}{h_{\mathrm{K(k)}} + h_{\mathrm{G,K(k)}}} \tag{36}$$

The mass-transfer rates at this interface are expressed by

$$\Gamma_{\mathrm{G,Lm}}^{\mathrm{I(G/K(k))}} = R_{\mathrm{Gm,K(k)}} \frac{q_{\mathrm{Gm,K(k)}}^{\mathrm{I}}}{i_{\mathrm{Gm}} - i_{\mathrm{Con,Gm}}} \tag{37}$$

Eq. (37) for m = 1, 2 and 3 is used for fuel, steel and sodium condensation, respectively.

At the interface between liquid fuel and liquid sodium, sodium vaporization can occur if the net heat flow is negative at the interface. The interfacial energy transfer rate is evaluated by

$$q_{\mathrm{L1,L3}}^{\mathrm{I}} = a_{\mathrm{L1,L3}}[h_{\mathrm{L1,L3}}(T_{\mathrm{L1,L3}}^{\mathrm{I}} - T_{\mathrm{L1}}) + h_{\mathrm{L3,L1}}(T_{\mathrm{L1,L3}}^{\mathrm{I}} - T_{\mathrm{L3}})] \tag{38}$$

The interface temperatures are expressed by

$$T_{\mathrm{L1,L3}}^{\mathrm{I}} = \max[T_{\mathrm{Sat,G3}}, T_{\mathrm{L1L3}}] \tag{39}$$

where the interface temperature, T_{L1L3}, in the case of no mass transfer is given by

$$T_{\mathrm{L1L3}} = \frac{h_{\mathrm{L1,L3}} T_{\mathrm{L1}} + h_{\mathrm{L3,L1}} T_{\mathrm{L3}}}{h_{\mathrm{L1,L3}} + h_{\mathrm{L3,L1}}} \tag{40}$$

The sodium vaporization rate at this interface is expressed by

$$\Gamma_{\mathrm{L3,G}}^{\mathrm{I(L1/L3)}} = -\frac{q_{\mathrm{L1,L3}}^{\mathrm{I}}}{i_{\mathrm{Vap,G3}} - i_{\mathrm{L3}}} \tag{41}$$

Similar treatment is applied to liquid-fuel/liquid-steel and liquid-steel/liquid-sodium interfaces, where steel and sodium vaporization can occur, respectively.

3.4. Closure relations

In SIMMER-III, the binary contact areas for 42 possible contact interfaces are determined based on the convective interfacial areas and a flow regime which describes the geometry of the multiphase flow [13]. Flow regimes are modeled for both pool flow, in which the effect of the structure is negligible, and channel flow, which is confined by structure. The heat-transfer coefficients are also determined for 42 binary contacts depending on the flow regime. The coefficients for solid particles, liquid droplets and gas bubbles are simply based on heat conduction, but the effects of internal circulation and oscillations are also considered for the fluid particles. The convective heat transfer in continuous fluids is formulated by empirical correlations for Nusselt numbers. Employing the heat- and mass-transfer analogy, the vapor-side mass-transfer coefficients independent of mass transfer can be found as a function of the Sherwood number from the empirical correlations developed for sensible heat transfer. For example, correlations for forced convection are generally in the forms:

$$\mathrm{Nu_g} = \frac{h_\mathrm{g} L}{\kappa_\mathrm{g}} = f(\mathrm{Re_g}, \mathrm{Pr_g}) \text{ and} \tag{42}$$

$$\mathrm{Sh_g} = \frac{k_\mathrm{g} L}{\rho_\mathrm{g} D_\mathrm{kg}} = f(\mathrm{Re_g}, \mathrm{Sc_g}) \tag{43}$$

where $\mathrm{Re_g} = \rho_\mathrm{g} v_\mathrm{g} L / \mu_\mathrm{g}$ and $\mathrm{Pr_g} = \mu_\mathrm{g} c_\mathrm{p.g} / \kappa_\mathrm{g}$. Necessary thermophysical and transport properties are calculated by an analytical model of SIMMER-III using general function forms for the reactor core materials [21].

3.5. V/C conservation equations and solution procedure

In the SIMMER-III fluid-dynamics solution algorithm, the V/C calculation performs intra-cell heat and mass transfer among liquid, vapor and solid phases after the interfacial areas and heat- and mass-transfer coefficients are obtained. The mass- and energy-conservation equations to be solved are written without convection for vapor mixture, three real liquids, and six solid components. The mass-conservation equations for vapor components are

$$\frac{\partial \overline{\rho}_{\mathrm{Gm}}}{\partial t} = \Gamma_{\mathrm{Lm,G}} - \Gamma_{\mathrm{G,Lm}}, \ \mathrm{m} = 1, 2 \text{ and } 3 \tag{44}$$

The energy-conservation equations are expressed in terms of specific internal energy:

for solid components

$$\frac{\partial \overline{\rho}_{\mathrm{K(k)}} e_{\mathrm{K(k)}}}{\partial t} = \sum_{\mathrm{m=1}}^{3} R_{\mathrm{Gm,K(k)}} a_{\mathrm{G,K(k)}} h_{\mathrm{K(k)}} (T^{\mathrm{I}}_{\mathrm{Gm.K(k)}} - T_{\mathrm{K(k)}}) + (1 - R_{\mathrm{G4,K(k)}}) a_{\mathrm{G,K(k)}} h_{\mathrm{K(k)}} (T_{\mathrm{GK(k)}} - T_{\mathrm{K(k)}}) \tag{45}$$

for real liquids

$$\frac{\partial \overline{\rho}_{\mathrm{L1}} e_{\mathrm{L1}}}{\partial t} = \Gamma_{\mathrm{G,L1}} i_{\mathrm{Con,G1}} - \Gamma_{\mathrm{L1,G}} i_{\mathrm{L1}} + \sum_{\mathrm{m=2}}^{3} a_{\mathrm{L1,Lm}} h_{\mathrm{L1,Lm}} (T^{\mathrm{I}}_{\mathrm{L1,Lm}} - T_{\mathrm{L1}})$$

$$+ R_{\mathrm{G1,L1}} a_{\mathrm{G,L1}} h_{\mathrm{L1,G}} (T^{\mathrm{I}}_{\mathrm{G1.L1}} - T_{\mathrm{L1}}) + (1 - R_{\mathrm{G1,L1}}) a_{\mathrm{G,L1}} h_{\mathrm{L1,G}} (T_{\mathrm{G4L1}} - T_{\mathrm{L1}}) \tag{46}$$

$$\frac{\partial \overline{\rho}_{\mathrm{L2}} e_{\mathrm{L2}}}{\partial t} = \Gamma_{\mathrm{G,L2}} i_{\mathrm{Con.G2}} - \Gamma_{\mathrm{L2,G}} i_{\mathrm{L2}} + a_{\mathrm{L1,L2}} h_{\mathrm{L2,L1}} (T^{\mathrm{I}}_{\mathrm{L1,L2}} - T_{\mathrm{L2}}) + a_{\mathrm{L2.L3}} h_{\mathrm{L2,L3}} (T^{\mathrm{I}}_{\mathrm{L2.L3}} - T_{\mathrm{L2}})$$

$$+ \sum_{\mathrm{m=1}}^{2} R_{\mathrm{Gm.L2}} a_{\mathrm{G,L2}} h_{\mathrm{L2,G}} (T^{\mathrm{I}}_{\mathrm{Gm,L2}} - T_{\mathrm{L2}}) + \left(1 - \sum_{\mathrm{m=1}}^{2} R_{\mathrm{Gm,L2}}\right) a_{\mathrm{G,L2}} h_{\mathrm{L2,G}} (T_{\mathrm{G4L2}} - T_{\mathrm{L2}}) \text{ and} \tag{47}$$

$$\frac{\partial \overline{\rho}_{\mathrm{L3}} e_{\mathrm{L3}}}{\partial t} = \Gamma_{\mathrm{G,L3}} i_{\mathrm{Con,G3}} - \Gamma_{\mathrm{L3,G}} i_{\mathrm{L3}} + \sum_{\mathrm{m=1}}^{2} a_{\mathrm{Lm,L3}} h_{\mathrm{L3,Lm}} (T^{\mathrm{I}}_{\mathrm{Lm.L3}} - T_{\mathrm{L3}})$$

$$+ \sum_{\mathrm{m=1}}^{3} R_{\mathrm{Gm.L3}} a_{\mathrm{G.L3}} h_{\mathrm{L3,G}} (T^{\mathrm{I}}_{\mathrm{Gm.L3}} - T_{\mathrm{L3}}) + \left(1 - \sum_{\mathrm{m=1}}^{3} R_{\mathrm{Gm.L3}}\right) a_{\mathrm{G.L3}} h_{\mathrm{L3,G}} (T_{\mathrm{G4L3}} - T_{\mathrm{L3}}) \tag{48}$$

for vapor mixture

$$\frac{\partial \overline{\rho}_{\mathrm{G}} e_{\mathrm{G}}}{\partial t} = \sum_{\mathrm{m=1}}^{3} \Gamma_{\mathrm{Lm.G}} i_{\mathrm{Vap.Gm}} - \Gamma_{\mathrm{G.Lm}} i_{\mathrm{Gm}} + \sum_{\mathrm{m=1}}^{3} R_{\mathrm{Gm.Lm}} a_{\mathrm{G,Lm}} h_{\mathrm{G,Lm}} (T^{\mathrm{I}}_{\mathrm{Gm.Lm}} - T_{\mathrm{G}})$$

$$+ R_{\mathrm{G1.L2}} a_{\mathrm{G.L2}} h_{\mathrm{G.L2}} (T^{\mathrm{I}}_{\mathrm{G1.L2}} - T_{\mathrm{G}}) + \sum_{\mathrm{m=1}}^{2} R_{\mathrm{Gm,L3}} a_{\mathrm{G.L3}} h_{\mathrm{G.L3}} (T^{\mathrm{I}}_{\mathrm{Gm,L3}} - T_{\mathrm{G}})$$

$$+\sum_{m=1}^{3}\sum_{k=1}^{6}R_{\mathrm{Gm,K(k)}}a_{\mathrm{G,K(k)}}h_{\mathrm{G,K(k)}}(T^{\mathrm{I}}_{\mathrm{Gm,K(k)}}-T_{\mathrm{G}})+\sum_{k=1}^{6}\left(1-\sum_{m=1}^{3}R_{\mathrm{Gm.K(k)}}\right)a_{\mathrm{G.K(k)}}h_{\mathrm{G.K(k)}}(T_{\mathrm{G4K(k)}}-T_{\mathrm{G}}) \tag{49}$$

The numerical solution procedure treats the vapor and the liquid coolant implicitly, but the other liquids and solid components are solved explicitly. The iteratively solved conservation equations are tightly coupled with EOSs. This is because of strong nonlinearity in phase-transition processes and a probable large change in the vapor thermodynamic state. In order to solve Eqs. (44) – (49), two types of variables are defined: "sensitive" and "less sensitive." The sensitive variables are comprised of three condensable vapor densities, the coolant energy and the vapor temperature. Vapor components participate directly in mass transfer, and hence it was judged best to solve changes in their values implicitly. The liquid fuel, liquid steel, particle and structure energies are the less sensitive variables. The sensitive variables are updated using a multivariate Newton-Raphson method. Following the convergence of the iteration, an explicit solution procedure is used for the remaining less sensitive variables.

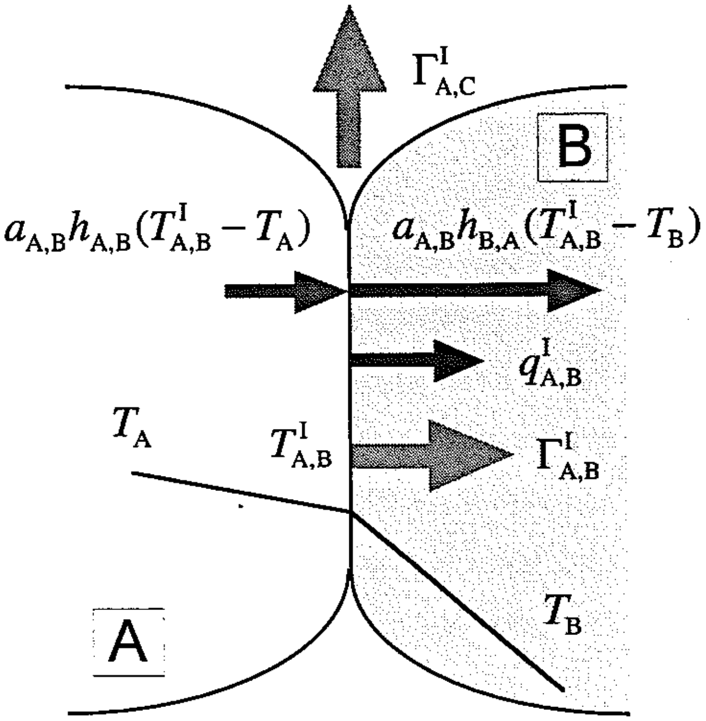

Fig. 1. Basis of nonequilibrium heat-transfer limited process.

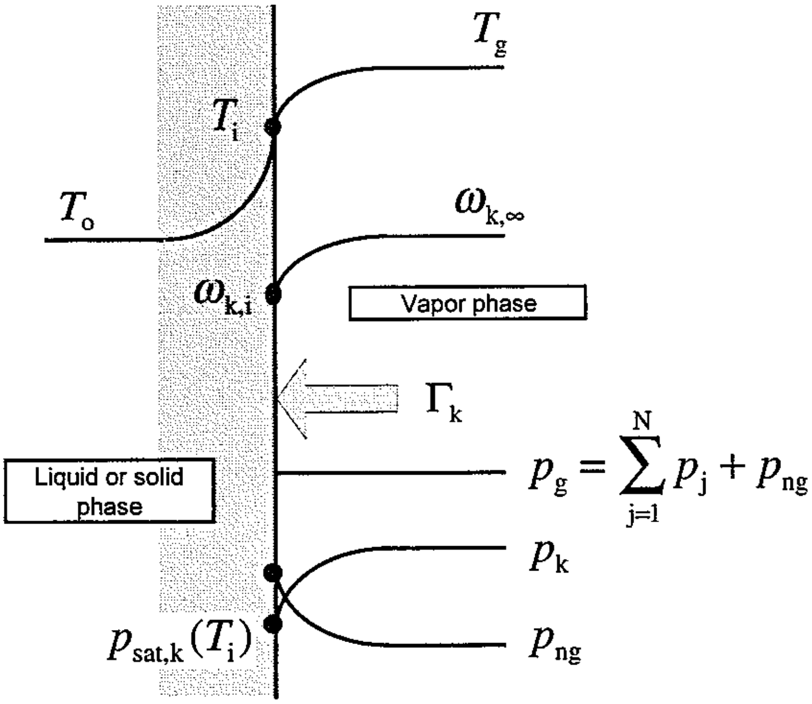

Fig. 2. Basis of mass-diffusion limited process.

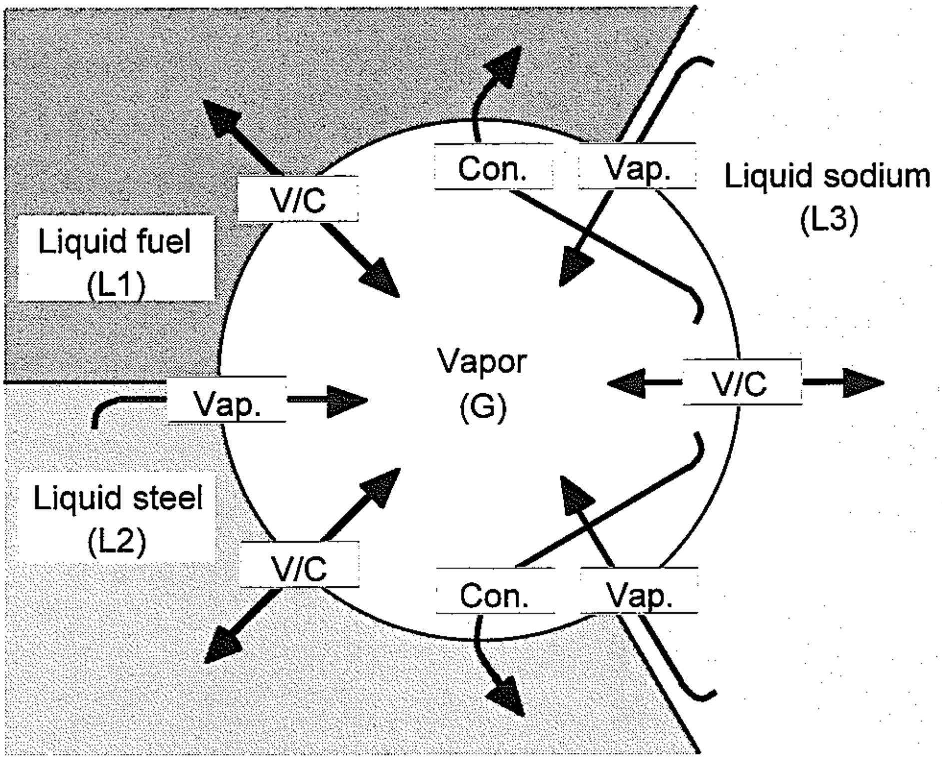

Fig. 3. Mass transfer processes occurring at liquid/liquid and vapor/liquid interfaces.

4. Basic model verification

Verification of the original model proposed for SIMMER-II has been performed using a series of multicomponent phase-transition experiments [22, 23]. Here, these experiments were re-calculated using SIMMER-III with the present V/C model to demonstrate its basic validity in the case of a single-component condensation with a noncondensable gas. The series of experiments, which is similar to an experimental study of pure-steam condensation by Dhir [24], has been performed by suddenly immersing a cold copper sphere of diameter 0.025 m in a large volume of vapor mixture. The steam was superheated to 408 K with variable amounts of air, helium or nitrogen as noncondensable gases. The steam condensed into a liquid film on the sphere under free- or forced-convection conditions, and then the sphere temperature rose due to the heat transfer through the condensate film. In the experiments, the temperature of the sphere center was recorded as a function of time. The experimental data are available in the range of quasi-steady condensation achieved after a sphere was immersed in the large volume of stagnant mixture.

For the SIMMER-III calculations, heat- and mass-transfer coefficients should be provided to close the constitutive equations. The liquid-side heat-transfer coefficient was found from the theoretical Nusselt number for laminar film condensation on a sphere [25]:

$$\mathrm{Nu}_\mathrm{o} = \frac{h_\mathrm{o} d}{2\kappa_\mathrm{o}} = 0.785\left[\frac{g\rho_\mathrm{o}(\rho_\mathrm{o}-\rho_\mathrm{g})i^*_\mathrm{lg} d^3}{\mu_\mathrm{o}\kappa_\mathrm{o}(T_\mathrm{i}-T_\mathrm{w})}\right]^{1/4} \tag{50}$$

where i^*_lg is the latent heat of vaporization corrected to account sensible heat of subcooling in the film, $i^*_\mathrm{lg} = i_\mathrm{lg} + 0.68 c_\mathrm{p,o}(T_\mathrm{i} - T_\mathrm{w})$. The physical properties used in Eq. (50) were evaluated at $T_\mathrm{w} + 0.3(T_\mathrm{i} - T_\mathrm{w})$. For the vapor-side heat–transfer coefficients, the following empirical relations for heat transfer from a sphere were used [20]:

$$\mathrm{Nu}_\mathrm{g} = 2 + 0.60(\mathrm{Gr}_\mathrm{g})^{1/4}(\mathrm{Pr}_\mathrm{g})^{1/3} \text{ for free convection, and} \tag{51}$$

$$\mathrm{Nu}_\mathrm{g} = 2 + 0.60(\mathrm{Re}_\mathrm{g})^{1/2}(\mathrm{Pr}_\mathrm{g})^{1/3} \text{ for forced convection} \tag{52}$$

The mass-transfer coefficients k_k were evaluated from the above Nusselt number correlations based on the analogy between heat and mass transfer:

$\mathrm{Sh}_g = 2 + 0.60(\mathrm{Gr}_g)^{1/4}(\mathrm{Sc}_g)^{1/3}$ for free convection, and (53)

$\mathrm{Sh}_g = 2 + 0.60(\mathrm{Re}_g)^{1/2}(\mathrm{Sc}_g)^{1/3}$ for forced convection (54)

In Eqs. (51) – (54), physical properties were evaluated at the film temperature $0.5(T_g + T_i)$ and the characteristic length L is set to the sphere diameter. In condensing system under free-convection conditions, the Grashof number Gr_g should be dependent on upon both temperature and composition differences, and was defined using the total density difference between bulk and the interface [26, 27]:

$$\mathrm{Gr}_g = \frac{g\rho_{g,\infty}(\rho_{g,\infty} - \rho_{g,i})L^3}{\mu_g^2} \tag{55}$$

The SIMMER-III calculations were performed as a zero-dimensional analysis with one computational cell.

The results of the experiment and the prediction in the case of the steam-air mixture under free-convection conditions are shown in Fig. 4. This figure indicates experimental measurements and predictions for the temperature rise of the sphere center with variable amounts of air present. Excellent agreement can be seen for the case of pure steam, where the liquid-side heat transfer dominates the condensation process. In the cases of air presence, the results show that the influence of air on condensation is remarkably large even if the steam-air mixture has only a low concentration of air. The process is limited by the mass diffusion, and thus the predictions depend on the mass-transfer coefficient, which was determined based on the heat- and mass-transfer analogy. Possible uncertainty in the mass-transfer coefficient could lead slightly poor agreement between the measurement and the predictions.

Figs. 5 and 6 indicate the SIMMER-III predictions of the vapor-liquid interface temperature and the correction factor, defined by Eq. (19), for the condensation rate. It can be seen from Fig. 5 that the results in the presence of air indicate considerable reduction in the interface temperature when the noncondensable gas accumulates at the liquid-vapor interface due to the mass transfer toward the interface. As the result, the rate of condensation is also reduced considerably when compared to the pure steam case. This reduction rate is equivalent to the correction factor shown in Fig. 6. In the prediction, the presence of only 1.8 % air reduces the interface heat flux or mass-transfer rate by nearly a factor of ten.

Experimental and analytical results for nitrogen and helium as the noncondensable gases in the mixture under forced-convection conditions are shown in Figs. 7 and 8, respectively. Compared with air and nitrogen, helium has the large difference in thermophysical properties, especially the mass-diffusion coefficient in the mixture. This results in the less noncondensable-gas effect of helium on condensation at the comparable concentration of the other noncondensable gases, as can be seen from the experimental data. However, SIMMER-III gives relatively large underestimation of the noncondensable-gas effect for high helium concentrations in the mixture. One of the reasons for this poor prediction might come from the simplification based on the analogy between the heat and mass transfer. In general, the analogy is valid when Prandtl number ~ Schmidt number, or Lewis number is equal to unity for the vapor mixture. However, under the present experimental conditions, the Lewis number of steam-helium mixture is about 0.18, while the Lewis numbers of steam-air and steam-nitrogen mixtures are about 0.65; the Lewis number of steam-helium mixture is much smaller than unity compared with those of the other mixtures. Nevertheless, it is encouraged that SIMMER-III with the present V/C model yields approximate solutions for variable amounts of and different species of noncondensable gas in the mixture.

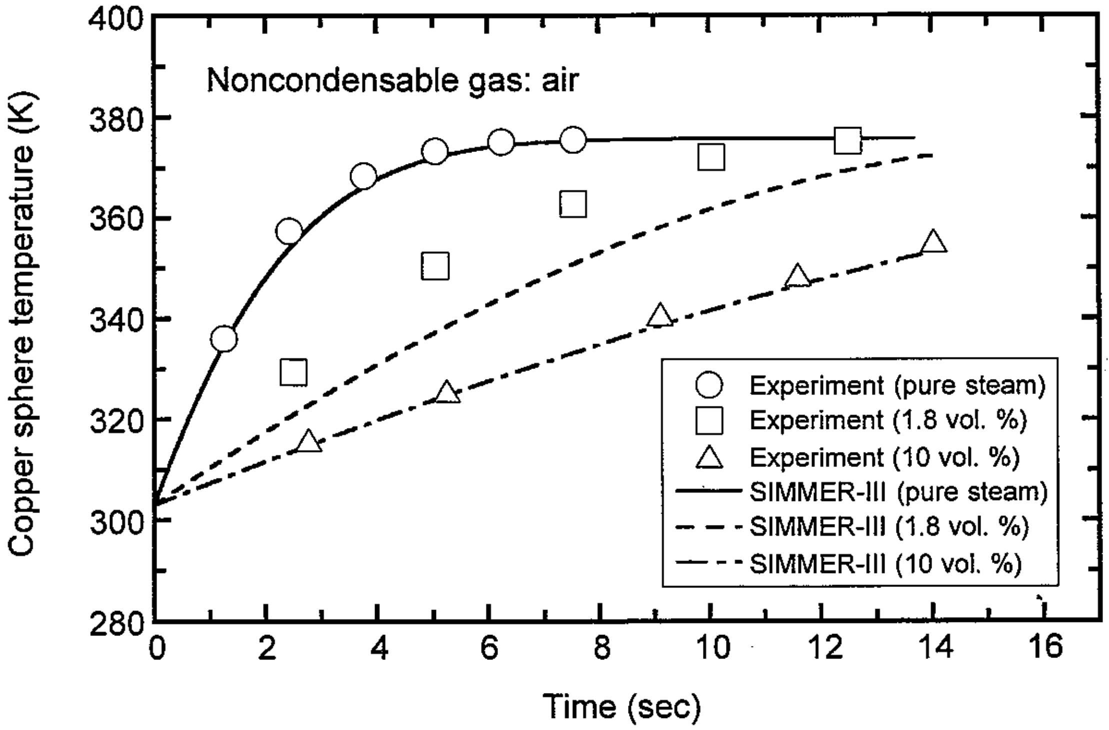

Fig. 4. Temperature rise of copper sphere in steam-air mixture.

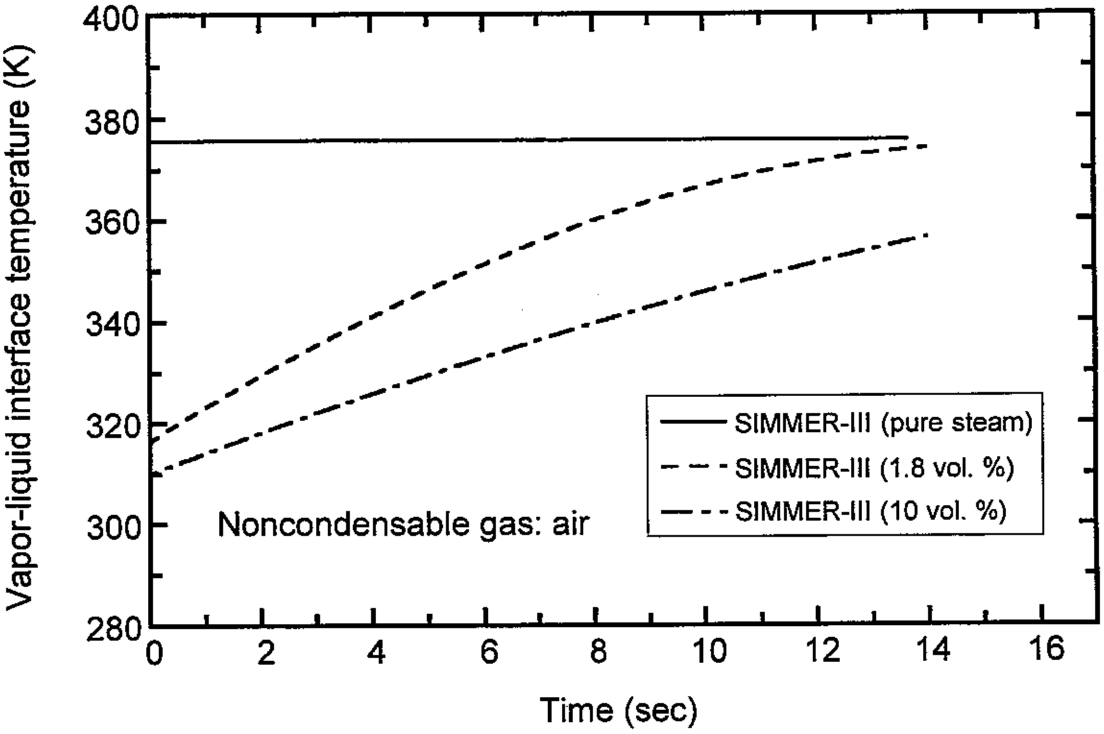

Fig. 5. Predictions of vapor-liquid interface temperature.

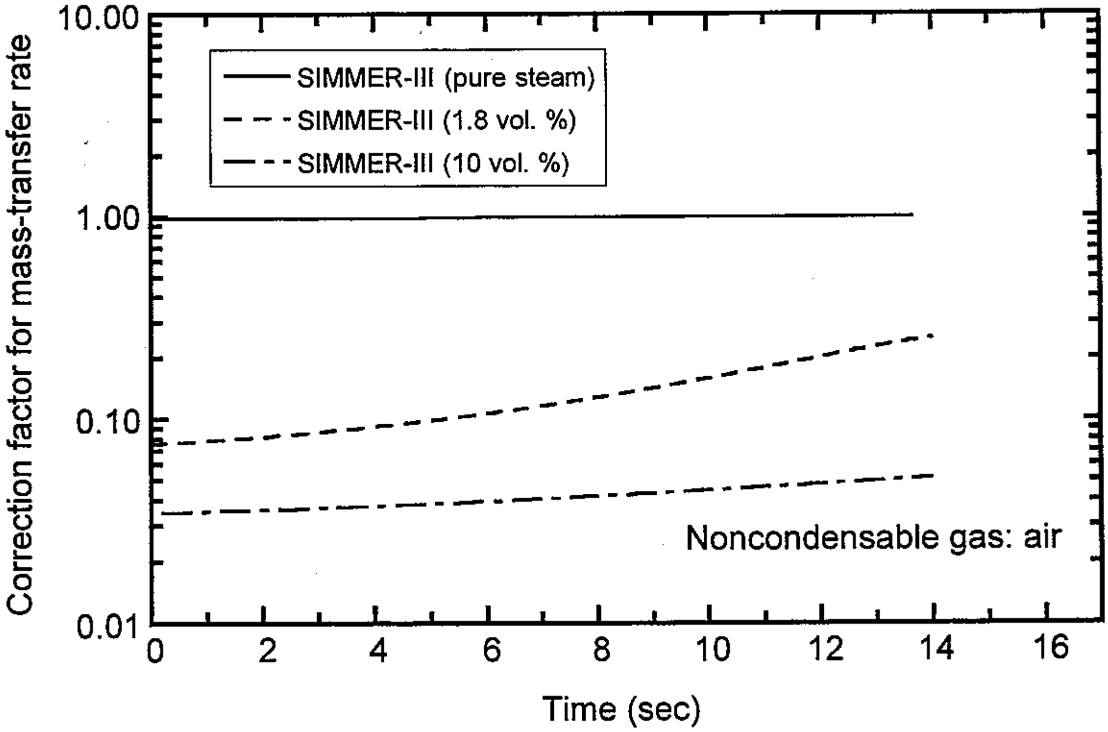

Fig. 6. Correction factor for steam condensation rate.

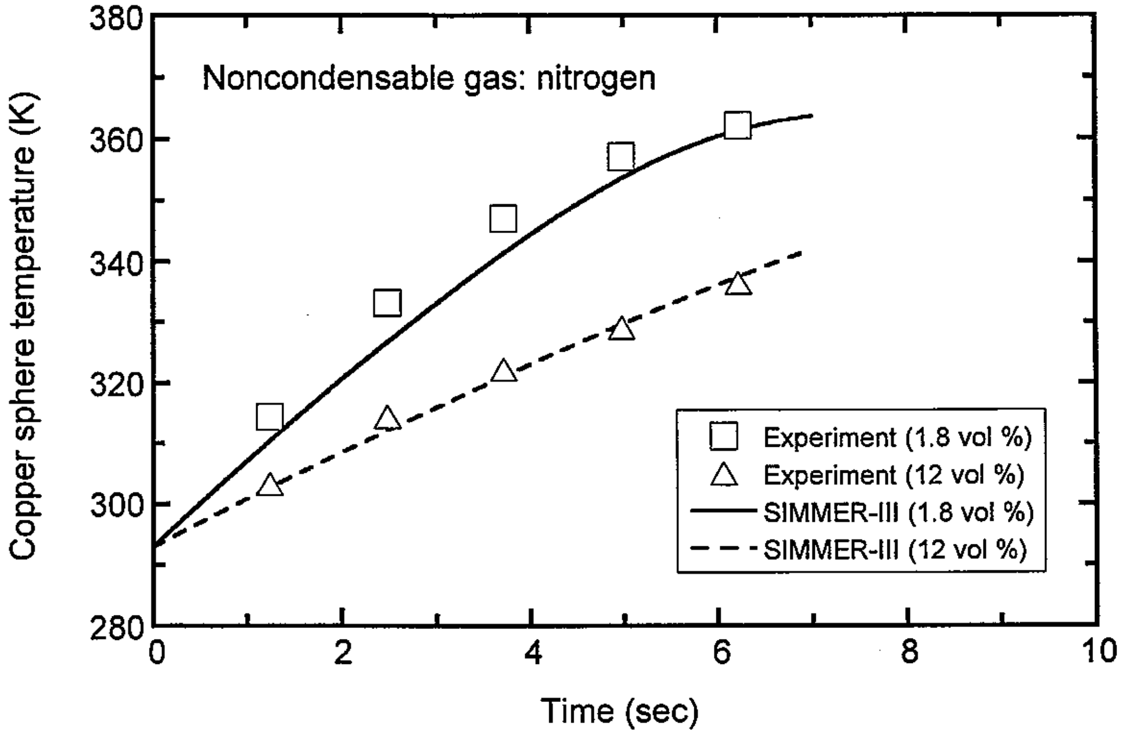

Fig. 7. Temperature rise of copper sphere in steam-nitrogen mixture.

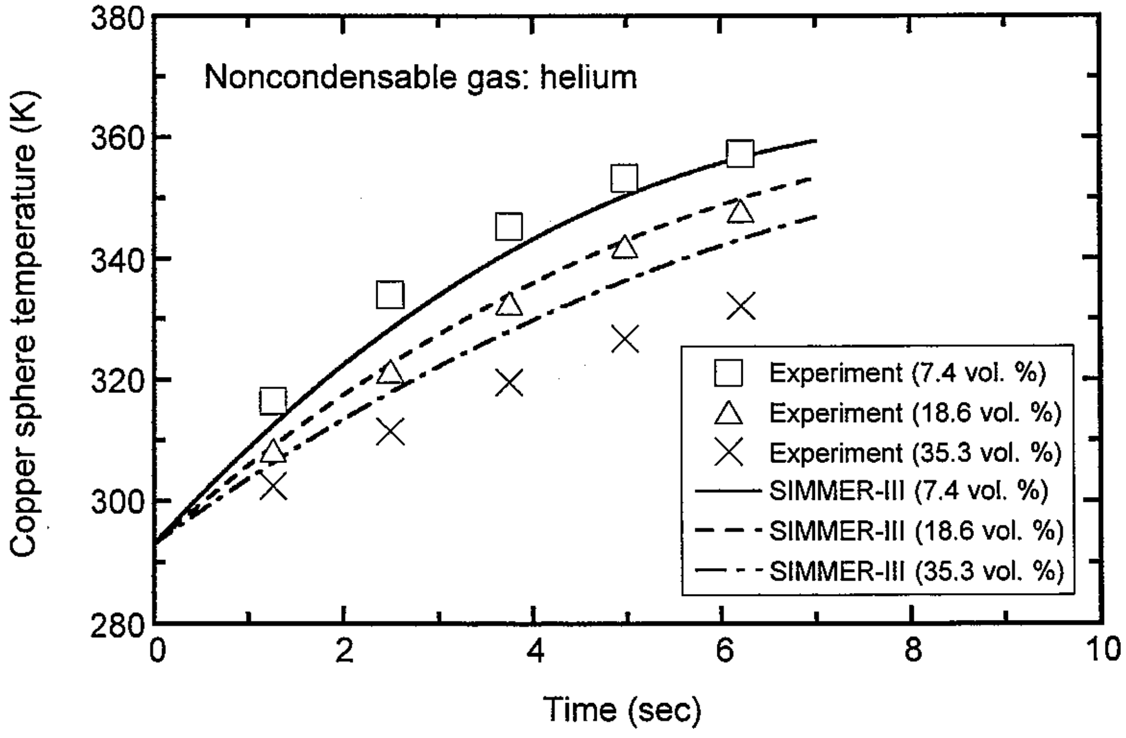

Fig. 8. Temperature rise of copper sphere in steam-helium mixture.

5. Extended model verification

Although the phase-transition model used in SIMMER-III has already been validated through many verification studies, most of such investigations were performed under the single-component phase transition: for example, the analysis of the condensation process of single-bubble in subcooled water [5]. In the previous chapter, basic validity of the newly developed multicomponent V/C model was successfully demonstrated by analyzing the condensation process of steam-noncondensable gas mixtures onto a copper sphere. It is also believed that more integrated model verification would be necessary to confirm the practical applicability of the present V/C model to the phase-transition process of multi-bubbles, which would be formed in a disrupted reactor core. However, there has been a lack of experimental data which could be used to directly confirm the applicability of the proposed V/C model in SIMMER-III to multi-bubble systems.

In the present study, a new series of condensation experiments of multi-bubbles including noncondensable components has been also performed for the extended model verification. In the experiments, number densities of bubbles, bubble diameters and void fractions are quantified using newly developed image-processing techniques. Moreover, the experimental results obtained through the image-processing techniques are compared with SIMMER-III analyses, in order to confirm the applicability of the new V/C model to multi-bubbles systems with noncondensable gas. Special features of the present study are not only making quantitative comparisons between experiments and numerical analyses, but also examining two-dimensional motions in bubbly flows with condensation.

In the experiments, a mixture of steam and noncondensable gas was injected into a thin rectangular water pool through nozzles. The noncondensable gases used were nitrogen or xenon. Then, two-dimensional flow patterns and bubble distributions in the pool were recorded directly as digital motion pictures. Quantitative information such as number densities, bubble diameters and void fractions were obtained from visualization images using image-processing tools, which were originally developed for the present work. The flow rates of steam and noncondensable gases and the subcooling of the water pool were taken as experimental parameters as well as a species of noncondensable gas.

5.1. Outline of experiment and measurement

A schematic view of the experimental apparatus is illustrated in Fig. 9. The test section was a rectangular tank made of Pyrex glass, whose inner width, height and depth were 300 mm, 500 mm and 30 mm, respectively. Five injection nozzles of 1.0 mm diameter were mounted at the tank bottom. The tank was filled with slightly subcooled water up to 360 mm from the nozzles exit. In this pool, two-dimensional bubbly flows with condensation were formed. A gas plenum with the gas injection nozzles was located at the bottom of the tank. A water jacket, in which hot water was heated with an electric heater and mixed with blades, was installed behind the tank. The temperature of pool water in the front tank was controlled by adjusting the power of the electric heater in the jacket.

Steam as the condensable component was made in a steam generator connected to the gas plenum. Nitrogen or xenon gas as the noncondensable component was supplied from a pressurized tank to the steam generator. The volume flow rate of steam G_A was measured by sampling the volume of condensed water which had overflowed from the pool, and that of noncondensable gas G_B was taken with a flow meter. During the visualizations, the settings of the electric heaters in the water jacket and in the steam generator were fixed at suitable values, so that there was minimal coalescence and breakup of the bubbles, and minimal overlap of bubbles on the visualization image. Temperatures of the pool water were measured by thermocouples before and after the visualizations.

The visualization images of bubbly flows were recorded as motion pictures with a digital video camera. During the visualization, back-lighting with a halogen lamp through polypropylene film was used in order to clarify the outlines of bubbles. Number densities of bubbles, bubble diameters and void fractions were obtained from the visualization images using the image-processing techniques. The digital motion picture files obtained in the visualization experiments must first be translated into a series of still frames using suitable applications. Media Studio made by Canopus Co. was used for this translation.

The image-processing program to obtain quantitative information from a series of still frames was developed from scratch using the rapid application development (RAD) tool Delphi ver. 5.0. A special feature of this image-processing program is that mesh cells corresponding to a SIMMER-III analysis can be set on the image, and that quantitative information such as number densities of bubbles, bubble diameters and void fractions can be output for each cell. Therefore, the results of the image processing can be directly compared with those of SIMMER-III analyses. Before using this program, background images without bubbles must be prepared.

The algorithm of the image-processing program is schematically depicted in Fig. 10. First, the bubbly flow image on the first still frame and the background image without bubbles must be input. Second, the mesh cell conditions corresponding to the SIMMER-III analysis are set up on the bubbly flow image. After these procedures, the background image is eliminated from the original bubbly flow image in order to clarify the shape of bubbles. This modified image is translated into a binary image, and then running numbers are assigned to individual bubble on the binary image as a labeling process. Fig. 11 shows an example of this binary process. The center-locations, diameters and volumes of each bubble are determined on the binary image, after which they are assigned into a matrix using the running numbers as a parameter. The methods for determining the bubble diameters and volumes will be described in the following section. When these procedures are completed for the first still frame, the same process is repeated for the next frame. When the number of frame-advances reaches a prescribed value, the time-smoothed number densities, bubble diameters and void fractions for each cell are output.

It was necessary to apply some hypotheses to the quantification of three-dimensional values, such as bubble diameters and void fractions, through two-dimensional images. In the present image-processing program, the bubble diameters were assumed to be circle-equivalent diameters on a two-dimensional binary image. In other words, the diameter of an actual bubble was defined as that of a circle, which had same area as a two-dimensional bubble image. Such a definition can be allowed, since only spherical and/or ellipsoidal bubbles were observed in the actual experiments. In addition, experimental conditions were carefully controlled so that the coalescence and breakup of bubbles hardly occurred, and there was minimal overlap of bubbles on the visualization images. Moreover, compared to the conventional drag coefficient model [28], in which sphere-equivalent bubble diameters are used, this assumption is generally acceptable, since realistic bubble diameters are taken neither in the present method nor in the conventional model.

The volumes of individual bubbles were also defined using the circle-equivalent diameters. Therefore, the void fractions can be given by dividing the total bubble volume assigned to a certain cell with the cell volume, which is the product of vertical mesh cell size L_x, horizontal one L_y and pool depth L_z. The adequacy and accuracy of the present image-processing results will be discussed in the next section.

5.2. Experimental results and discussions

In the condensation experiments, bubble behaviors in the rectangular pool varied according to the concentration of the noncondensable gas. Fig. 12 shows actual photographs taken in the condensation experiment using nitrogen as the noncondensable gas. These photographs were obtained under the conditions of 1.9 ~ 1.1 K in pool water subcooling and 670 ~ 680 *l*/h of total gas flow rate G_{M}. The nitrogen concentration in Fig. 12 (a), (b) and (c) were 0, 0.07 and 0.71 vol. %, respectively. For pure steam condensation, multi-bubbles injected through the nozzle rose almost vertically and condensed completely. On the other hand, the steam-nitrogen mixture bubbles did not disappear completely. Under the condition of Fig. 12 (b) and (c), a remarkable oscillatory behavior of bubbly flow was observed through the bubble distribution. Before using the present method to quantify the number densities, the bubble diameters and the void fractions from these visualization images, the adequacy and accuracy of the image-processing results should be examined.

The accuracy of quantification for the bubble diameters through the present image-processing techniques was confirmed using opaque spherical particles of steel instead of moving bubbles. The steel particles were suspended with transparent threads in the water pool. The diameters of the particles obtained through the image-processing techniques were compared with those measured directly using a slide caliper. They agreed within the accuracy of ± 2 %. This fact suggests that the present tools are adequate to take the outlines of bubbles on the visualization images, or to determine the bubble diameters.

In order to validate the quantification of void fractions using the present method, a series of preliminary experiments without condensation was performed, in which only nitrogen gas was injected into the pool to form bubbly flows. The void fractions obtained in the preliminary experiments through image processing were compared with those predicted by the conventional drift correlation and those calculated by SIMMER-III. The comparisons are shown in Fig. 13, where pool-average void fractions, α_p, were evaluated as space- and time-average values for 10 sec. The image-processing results are plotted with circles in Fig. 13.

The curved line in this figure shows the predictions for pool-averaged void fractions using ordinary drift correlations given by the following equation:

$$\alpha_\mathrm{p} = \frac{j_\mathrm{g}}{C_0 j_\mathrm{g} + V_\mathrm{gj}} \tag{56}$$

where j_g is the volumetric gas flux calculated from gas flow rate, and C_0 and V_gj are the distribution parameter and drift velocity, respectively [28]. For the rectangular pool as used in the present work C_0 is given by

$$C_0 = 1.35 - 0.35\sqrt{\frac{\rho_\mathrm{g}}{\rho_\mathrm{f}}} \tag{57}$$

For bubbly flows including deformed ellipsoidal bubbles as seen in the present experiments, V_gj is given by following equation [29]:

$$V_\mathrm{gj} = \sqrt{2}\,(1-\alpha_\mathrm{p})^{1.75}\left(\frac{\sigma g\,\Delta\rho}{\rho_\mathrm{f}^2}\right)^{0.25} \tag{58}$$

Eq. (58) is approximately equivalent to the drift velocity correlation used in the momentum exchange model of SIMMER-III.

Comparing the image-processing results of the preliminary experiments with the curve line expressing the drift correlation, the void fractions in the experiments are slightly smaller than those predicted by the drift correlation. The reason is that the conventional drift correlation for one-dimensional flows includes no effect of liquid circulations due to multi-bubble rising, which decreases the pool-average void fractions in the thin rectangular pool.

On the other hand, the void fractions obtained in the preliminary experiments can be suitably represented by SIMMER-III analyses, whose detail will be described in Section 5. Although the drift velocity correlation similar to Eq. (58) is also used in the momentum exchange model of SIMMER-III, the analytical results can take the two-dimensional circulation effects into account. Therefore, the SIMMER-III analyses have good agreement with the experiments. Moreover, it has been already confirmed through many verification studies [13, 30] that SIMMER-III can represent various flow characteristics including multi-bubbles without condensations. Therefore, the fact that the void fractions obtained in the preliminary experiments can be reasonably reproduced by SIMMER-III supports the good adequacy and accuracy of the present image-processing methods for the void fraction measurements.

In the actual behavior of bubbly flows, the spatial distribution of individual bubbles may change with time as described for Fig. 12 (b) and (c). Therefore, in the quantification of number densities, bubble diameters and void distributions as verification data for SIMMER-III, time-smoothed values are required. An examination of the sampling time, that is, the number of still-frame images processed to obtain time-smoothed values, is necessary. Fig. 14 shows the number distributions of bubbles $n(y)$, for various sampling times, where $n(y)$ was determined by counting the number of bubbles assigned to a certain band of height L_y. In Fig. 14, the number distribution $n(y)$ was obtained under the same condition as Fig. 12 (b).

It can be seen that $n(y)$ distribution becomes almost flat with increased sampling time. In addition, there is no obvious difference between time-smoothed $n(y)$ over 10 sec and that over 30 sec. Therefore, the time-smoothed values for 10 sec are used as image-processing results in the present paper. Moreover, the flat distribution of $n(y)$ in Fig. 14 suggests that coalescence and breakup of bubbles hardly occurs along the vertical direction.

Before describing the actual results obtained from the condensation experiments including noncondensable gas, the relationship among the number density of bubbles $N(y)$, the bubble diameter $D_b(y)$ and the void fraction $\alpha(y)$ should be checked. In general, the following relation should be satisfied:

$$\frac{\pi}{6}\{D_b(y)\}^3 = \frac{\alpha(y)}{N(y)} \tag{59}$$

The number density is expressed as

$$N(y) = \frac{n(y)}{n_x L_x L_y L_z} \tag{60}$$

where n_x is the number of cells in the horizontal direction.

Fig. 15 shows the comparison of the bubble diameters measured directly through the image processing with those calculated from Eq. (59). The experimental values of $D_b(y)$, $N(y)$ and $\alpha(y)$ used in this figure were obtained in the actual condensation experiments for steam-nitrogen system. From Fig. 15, it can be seen that the measured and calculated diameters agree within an accuracy of 10 %. This fact also suggests that the quantification methods used in the present image-processing techniques have adequate accuracy.

The actual data obtained in the condensation experiments for various concentrations and species of noncondensable gas will be presented in Section 6.4 for the comparisons with SIMMER-III analytical results.

5.3. *Experimental analysis*

The conservation equations for mass, momentum and energy used in SIMMER-III are described for multicomponent systems [31, 32]. Rewriting them for the two-component systems as discussed in the present study, the mass-conservation equations for gas and liquid are:

$$\frac{\partial \bar{\rho}_g}{\partial t} + \nabla \cdot (\bar{\rho}_g \mathbf{v}_g) = -\Gamma_A \tag{61}$$

$$\frac{\partial \bar{\rho}_f}{\partial t} + \nabla \cdot (\bar{\rho}_f \mathbf{v}_f) = \Gamma_A \tag{62}$$

the momentum equations are:

$$\frac{\partial \bar{\rho}_g \mathbf{v}_g}{\partial t} + \nabla \cdot (\bar{\rho}_g \mathbf{v}_g \mathbf{v}_g) = -\alpha_g \nabla p + \bar{\rho}_g \mathbf{g} + K_{gf}(\mathbf{v}_f - \mathbf{v}_g) - \Gamma_A \mathbf{v}_g + \mathbf{VM}_g \tag{63}$$

$$\frac{\partial \bar{\rho}_f \mathbf{v}_f}{\partial t} + \nabla \cdot (\bar{\rho}_f \mathbf{v}_f \mathbf{v}_f) = -\alpha_f \nabla p + \bar{\rho}_f \mathbf{g} + K_{fg}(\mathbf{v}_g - \mathbf{v}_f) + \Gamma_A \mathbf{v}_f + \mathbf{VM}_f \tag{64}$$

and the energy equations are:

$$\frac{\partial \bar{\rho}_g e_g}{\partial t} + \nabla \cdot (\bar{\rho}_g e_g \mathbf{v}_g) = -p\left[\frac{\partial \alpha_g}{\partial t} + \nabla \cdot (\alpha_g \mathbf{v}_g)\right] + K_{gf}(\mathbf{v}_f - \mathbf{v}_g) \cdot (\mathbf{v}_f - \mathbf{v}_g)$$

$$-\Gamma_A (i_{fg,A} + i_g) + \mathbf{VM}_g \cdot (\mathbf{v}_f - \mathbf{v}_g) + a_i h_g (T_i - T_g) - p\frac{\partial \alpha_g}{\partial t} \tag{65}$$

$$\frac{\partial \bar{\rho}_f e_f}{\partial t} + \nabla\cdot(\bar{\rho}_f e_f \mathbf{v}_f) = -p\left[\frac{\partial \alpha_f}{\partial t} + \nabla\cdot(\alpha_f \mathbf{v}_f)\right] + K_{fg}(\mathbf{v}_g - \mathbf{v}_f)\cdot(\mathbf{v}_g - \mathbf{v}_f)$$

$$+\Gamma_A(i_{gf,A} + i_f) + \mathbf{VM}_f\cdot(\mathbf{v}_g - \mathbf{v}_f) + a_i h_f(T_i - T_f) - p\frac{\partial \alpha_f}{\partial t} \qquad (66)$$

where $K_{qq'}$ is the momentum exchange function between gas and liquid phases, and **VM** is the virtual mass term. The condensation rate Γ_A appearing in the above conservation equations is evaluated through the heat-transfer and mass-diffusion models described in Chapter 3.

In the SIMMER-III calculations, the rectangular pool with cover gas was modeled by a two-dimensional Cartesian geometry. A schematic view of the geometry used in the present analyses is illustrated in Fig. 16. The geometry, whose width and height were 300 mm and 400 mm, consisted of 37 horizontal- and 50 vertical- computational cells. Cell sizes in the vertical direction L_y, were 8 mm, and those in horizontal direction L_x, were also 8 mm, except at both ends where they were 10 mm. Since the experimental liquid level was 360 mm from the nozzle exit, it was assumed that the lower 45 cells were filled with single-phase water and the upper 5 cells were occupied with nitrogen or xenon as a cover gas at the beginning of the calculation. The temperature of the pool water in the tank was adjusted to experimental measurements. The pressure at the top boundary was assumed equal to atmospheric pressure P_0 and that at the bottom boundary was assumed the sum of P_0 and hydrostatic head pressure.

A gas mixture of steam and noncondensable component was supplied uniformly from the central 25 cells at the bottom, with a combined width of 200 mm. The volumetric gas flow rate G_M and the concentration of the noncondensable gas were based on experimental data. Temperature of the gas mixture supplied from the bottom was assumed to be saturated one at the bottom-boundary pressure. The velocity of the gas phase at the bottom boundary was assumed as

$$V_g(0) = L_y\, G \Big/ \left[\frac{\pi}{6}\, D_{b2}{}^3 \left\{N_2\left(n_x L_x L_y L_z\right) - 1\right\}\right] \qquad (67)$$

where D_{b2} and N_2 were the mean bubble diameter and the number density in the second lowest cell obtained by the image processing, respectively. The reason why D_{b2} and N_2 are used in the above equation will be discussed in the next section. The void fraction at the bottom boundary used in the present analyses was expressed as:

$$\alpha(0) = j_g / V_g(0) \tag{68}$$

The initial bubble diameter at the boundary was defined by the following equation:

$$D_b(0) = \left[\left(n_{\mathrm{nozzle}} L_x L_y L_z \right) \alpha(0) \Big/ \left\{ \frac{\pi}{6} \cdot N_1 \left(n_x L_x L_y L_z \right) \right\} \right]^{1/3} \tag{69}$$

where N_1 was number density in the lowest cell obtained from experiment. The number of the injection nozzles n_{nozzle}, was five. Incidentally, since the coalescence and breakup of bubbles were scarcely seen in the actual experiment, consequent changes of interfacial area were not taken into account in the analyses.

The time-smoothed values of the number densities, mean bubble diameters and the void fractions from analyses were obtained by averaging analytical results over 10 sec after quasi-static states were established.

5.4. Comparison between experiment and analysis

In the present SIMMER-III analyses, the effects of noncondensable-gas concentrations and species on the condensation process were examined. Two-dimensional flow patterns with multi-bubble condensations as observed in the experiment were also examined.

The vertical distribution of the number densities $N(y)$, the mean bubble diameters $D_b(y)$ and the average void fractions $\alpha(y)$ for various nitrogen concentrations are compared between SIMMER-III predictions and experimental results in Figs. 17, 18 and 19, respectively. Here, the experimental data were obtained under the conditions of pool water subcooling of 1.9 ~ 1.1 K and steam flow rate of 670 ~ 680 *l*/h. The number densities, the bubble diameters and the void fractions were evaluated as lateral- and time-averaged values for 10 sec. The distributions of $D_b(y)$ and $\alpha(y)$ obtained in the experiments increase once and then decrease in proportion to the height from nozzle exit. The reason why the experimental distributions have peaks just after the injection may be that bubbles begin condensation before they have fully grown. Since the present model verification study addresses the multi-bubble condensation process, the experimental data during the developing stage of bubble growth were neglected for the verification. This is the reason why D_{b2} and N_2 are used in Eq. (17) in order to estimate the boundary gas velocity.

For pure steam condensation, multi-bubbles injected from the bottom boundary condense completely at about 100 mm from the bottom. On the other hand, the size of steam-nitrogen mixture bubbles becomes a non-zero value, which depends on nitrogen concentration, during their condensation. It can be seen that the vertical distributions are appropriately represented by SIMMER-III using the present V/C model for various amounts of nitrogen. SIMMER-III predicts the definite differences in $D_b(y)$ and $\alpha(y)$ depending on the nitrogen concentration, which are much larger than experimental uncertainty.

The effect of the thermophysical properties of noncondensable gas on multi-bubble condensation was also investigated by comparison between steam-nitrogen and steam-xenon mixtures. Fig. 20, 21 and 22 shows the results for 0.71 vol. % concentration of noncondensable gas. Here, the experimental data were obtained under the conditions of pool water subcooling of 1.8 ~ 1.6 K and steam flow rate of 670 *l*/h. As shown in these figures, the condensation rate in the steam-xenon system becomes smaller than that in the steam-nitrogen one, due to the large molecular weight of xenon compared to that of nitrogen. In other words, the mass-transfer resistance for the diffusion of steam toward the interface in the steam-xenon system is larger than that in the steam-nitrogen one. SIMMER-III also suitably reproduces this effect of the noncondensable gas properties.

In the experiment, a peculiar oscillatory behavior of multi-bubble motion was observed in the rectangular pool. This is a two-dimensional flow pattern in the bubble condensation as shown in Fig. 23. The observed transient of two-dimensional void distributions is indicated as a series of void-fraction contours in Fig. 23 (a), which was obtained through the image-processing techniques. Fig. 23 (b) shows the SIMMER-III results corresponding to the observation. A similar two-dimensional oscillatory motion with a cycle of about 16 sec, which is comparable to the observation, is well reproduced by SIMMER-III. SIMMER-III with the present V/C model represents not only the condensation rate of multi-bubbles, but also their fluid motion in the rectangular pool.

5.5. Application to the reactor case

The verified V/C model was applied to the PDE (Post-Disassembly Expansion phase) of a typical FBR model plant with fuel inventory of about 7 ton and thermal power of 1600 MWth to investigate the effect of the mass-diffusion limited V/C model in comparision with the ordinary heat-trasnfer limited V/C model in SIMMER-III and also to check the practical robustness of the model. The analytical system is shown in Fig. 24. The time transients of the mechanical energy, which is the sum of the kinetic energy of sodium slug in the upper plenum and the PΔV work of cover gas, were plotted in Fig. 25 through the PDE analysis. The calculated maximum mechanical energy using the heat-trasnfer limited V/C model is 47.5 MJ whereas 49.4 MJ is obtained by mass-diffusion limited model. It can be said that the mechanical energy release is increased by about 2 MJ as the result of the suppression of sodium vapor condensation to the bubble surface which is modeled by the mass-transfer limited model. This application study indicates that the code could simulate the effects of multicomponent mixture on the phase transition practically although the effect of the difference of the V/C model is not so large in this sample case since the pressure in the bubble has a tendency to be kept by the sodium vapor supply by the FCI in the upper plenum.

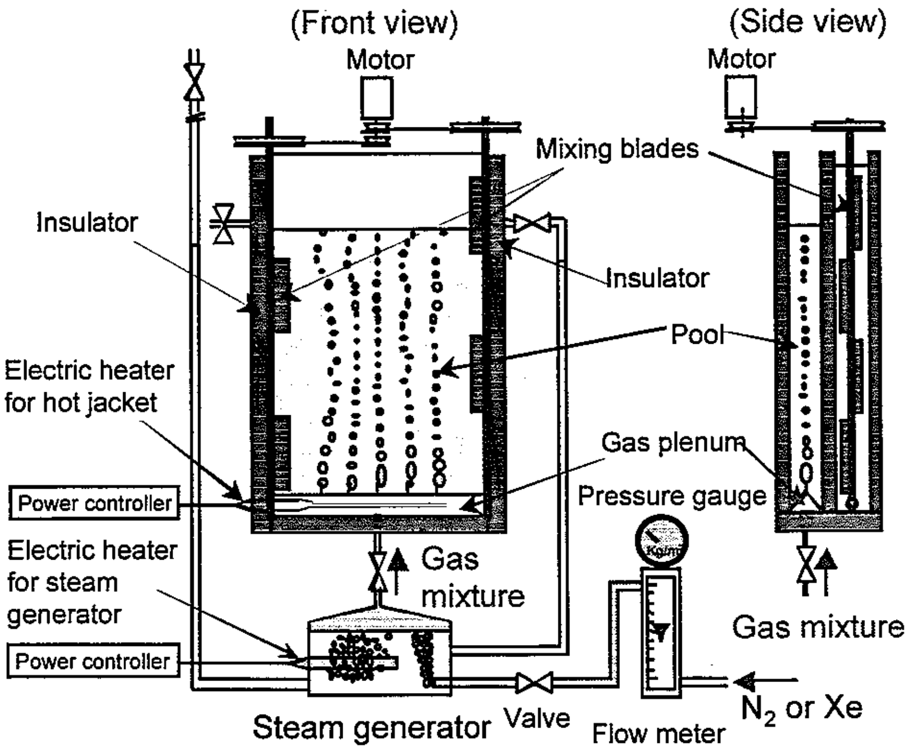

Fig. 9. Experimental apparatus.

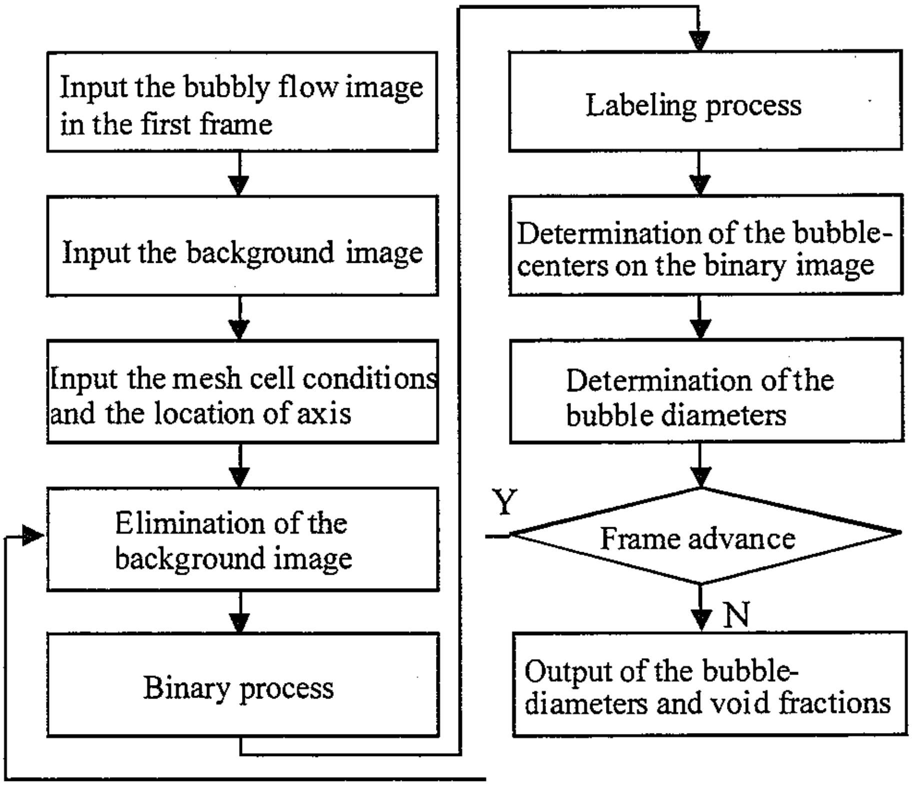

Fig. 10. Flow chart of the image-processing program.

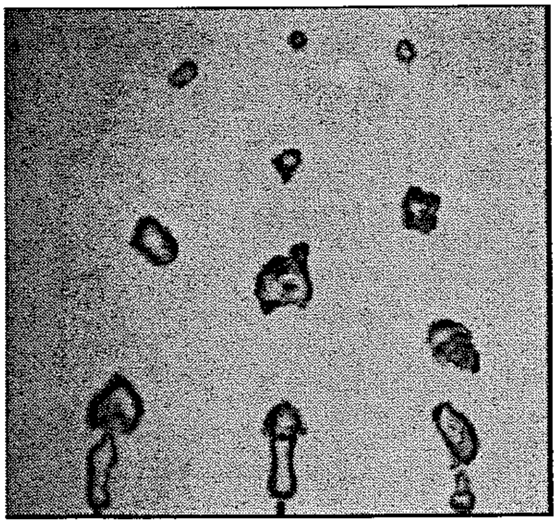

(a) original image

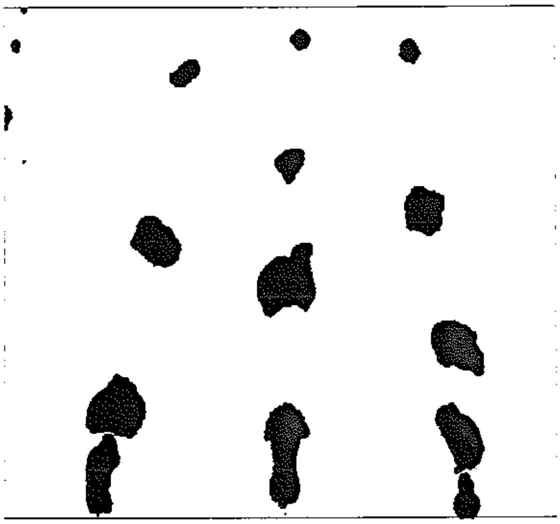

(b) binary image

Fig. 11. Example of the binary process.

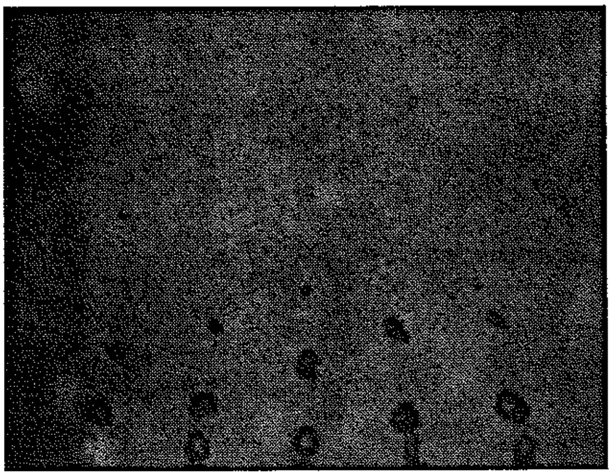

(a) pure steam

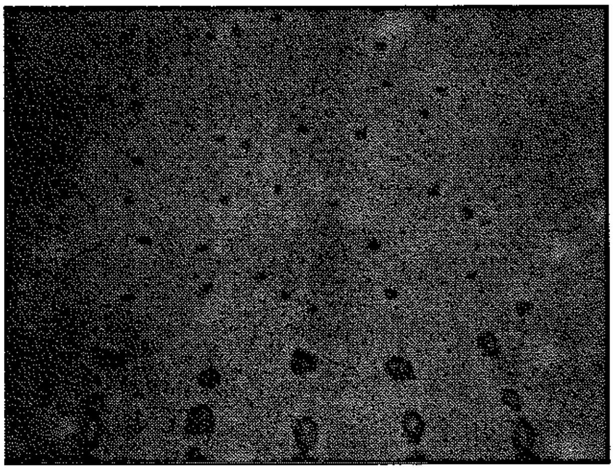

(b) concentration of nitrogen: 0.07 vol. %

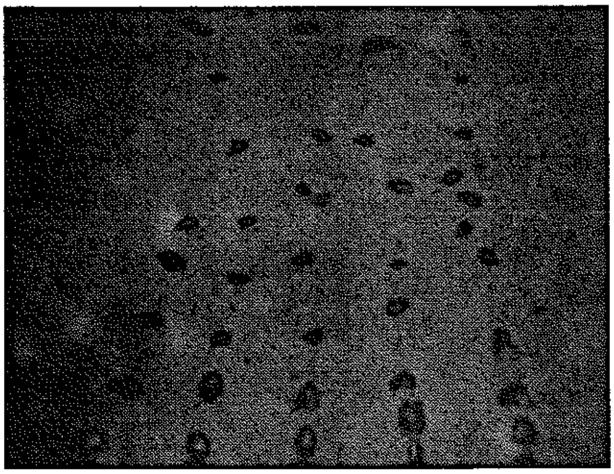

(c) concentration of nitrogen: 0.71 vol. %

Fig. 12. Photographs of the condensation process in bubbly flows.

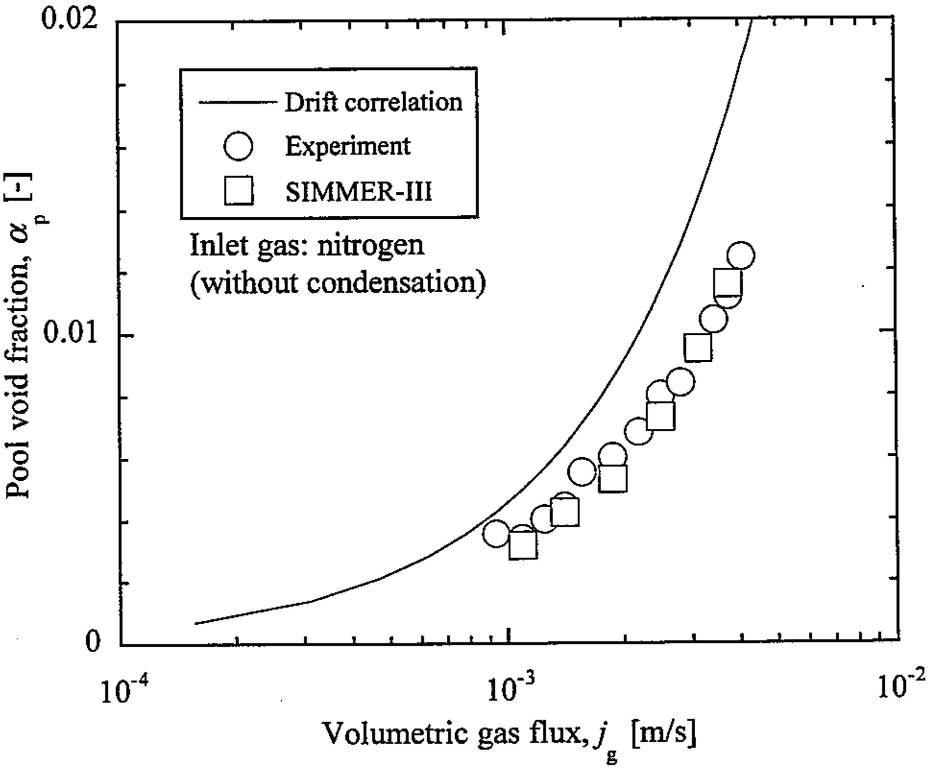

Fig. 13. Calibration for the void-fraction measurements.

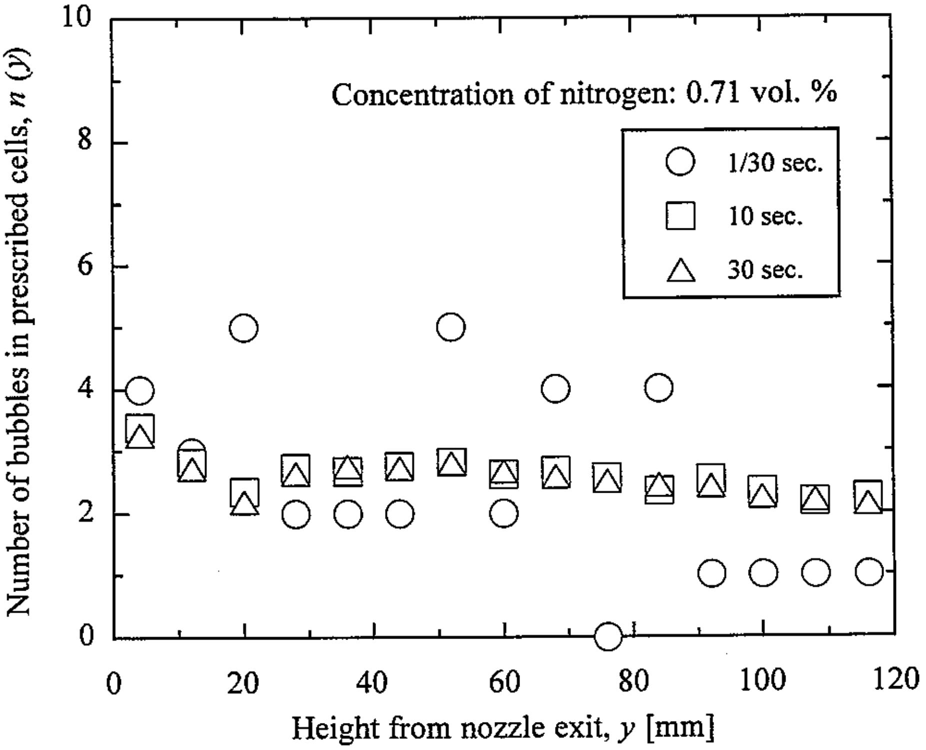

Fig. 14. Effect of the sampling time on the distributions.

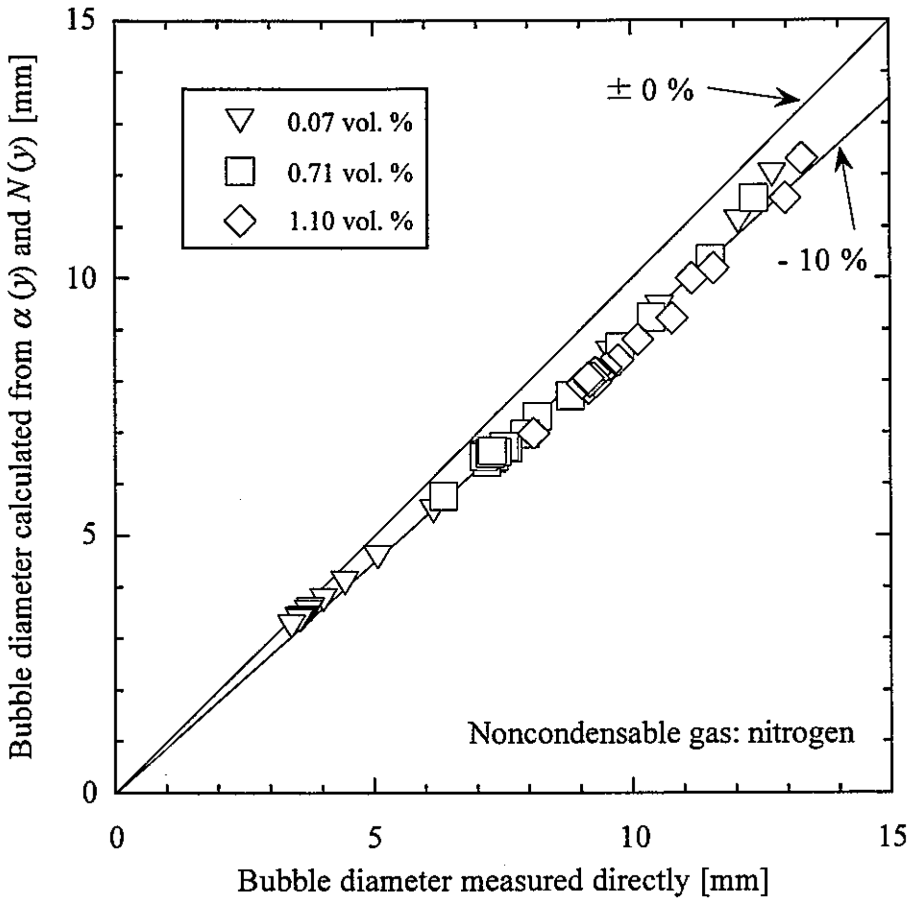

Fig. 15. Comparison of the bubble diameters to confirm the image-processing validity.

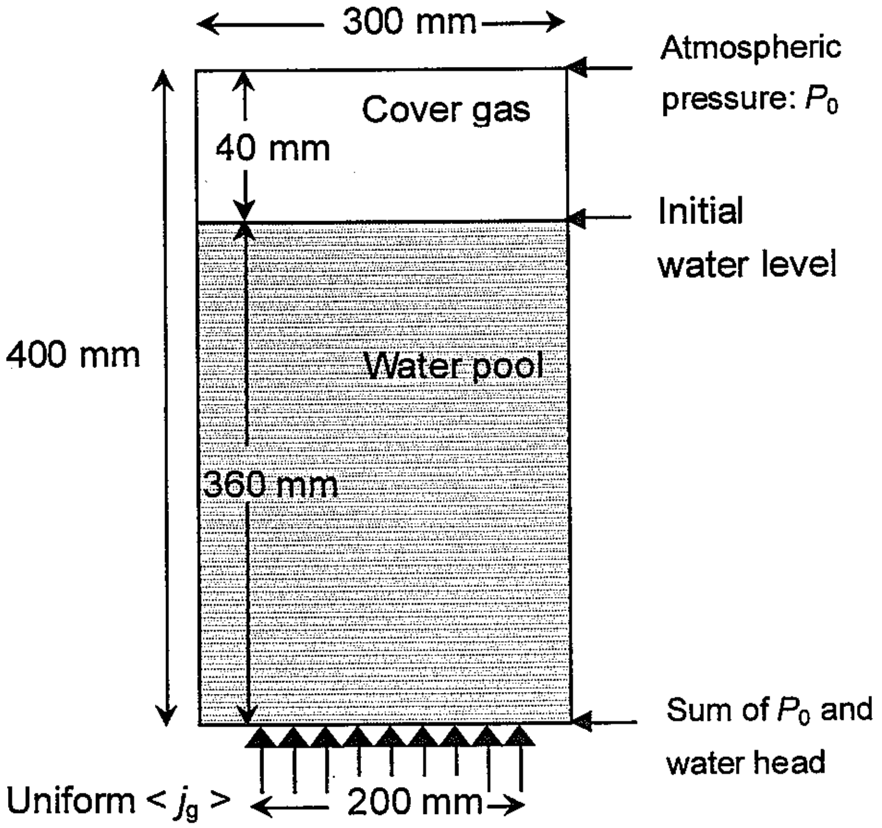

Fig. 16. Geometric model for analysis.

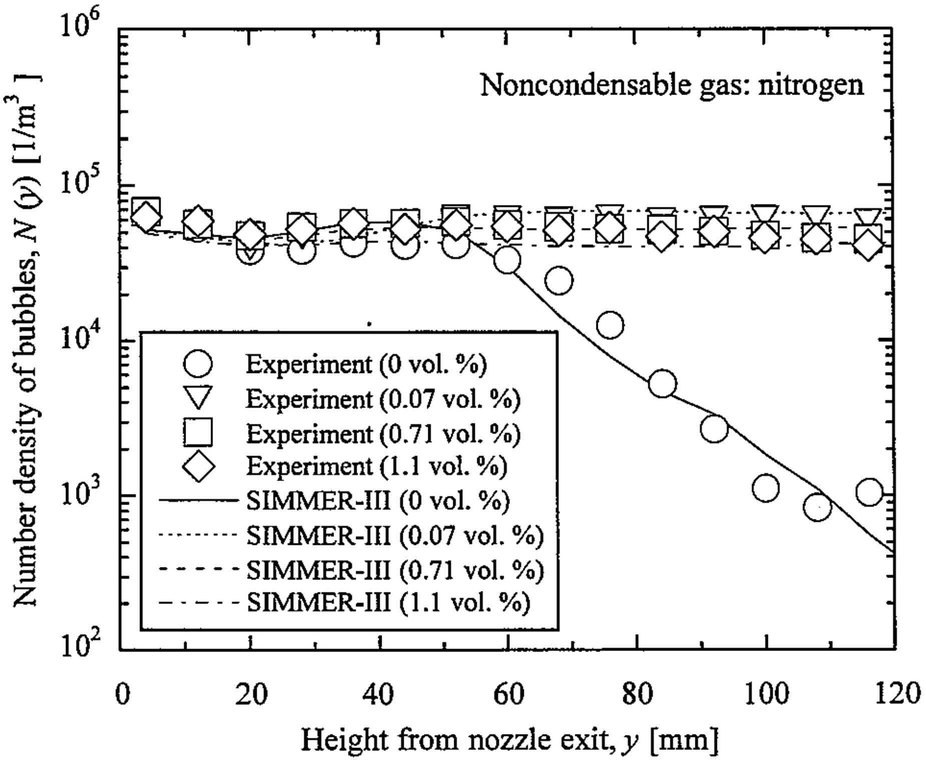

Fig. 17. Vertical distributions of number densities for various nitrogen-concentrations.

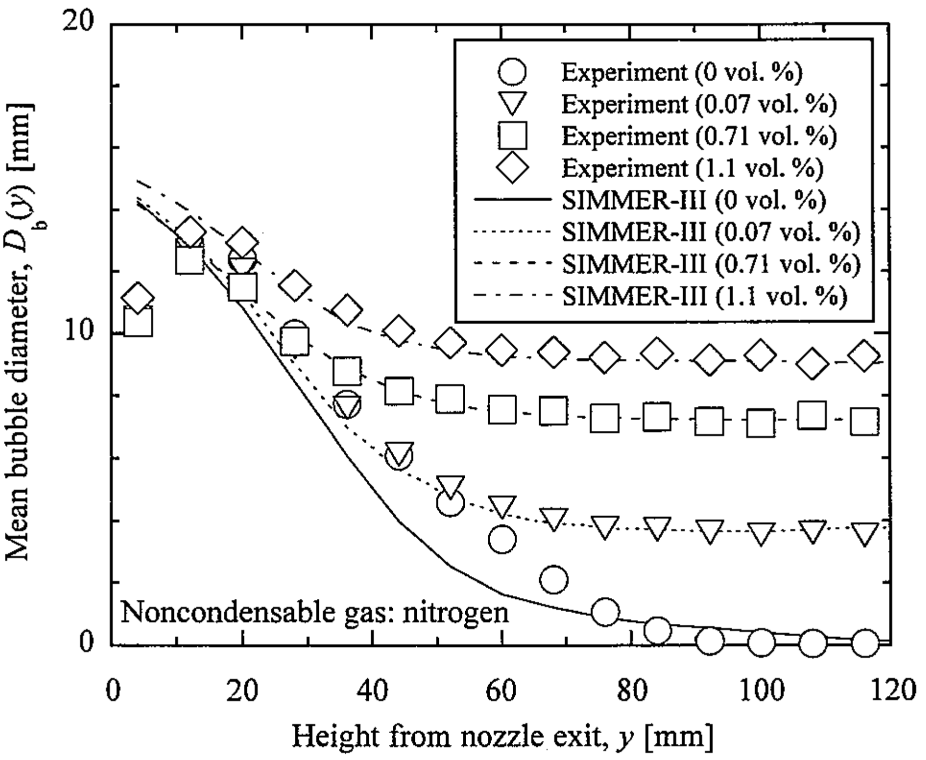

Fig. 18. Vertical distributions of bubble diameters for various nitrogen-concentrations.

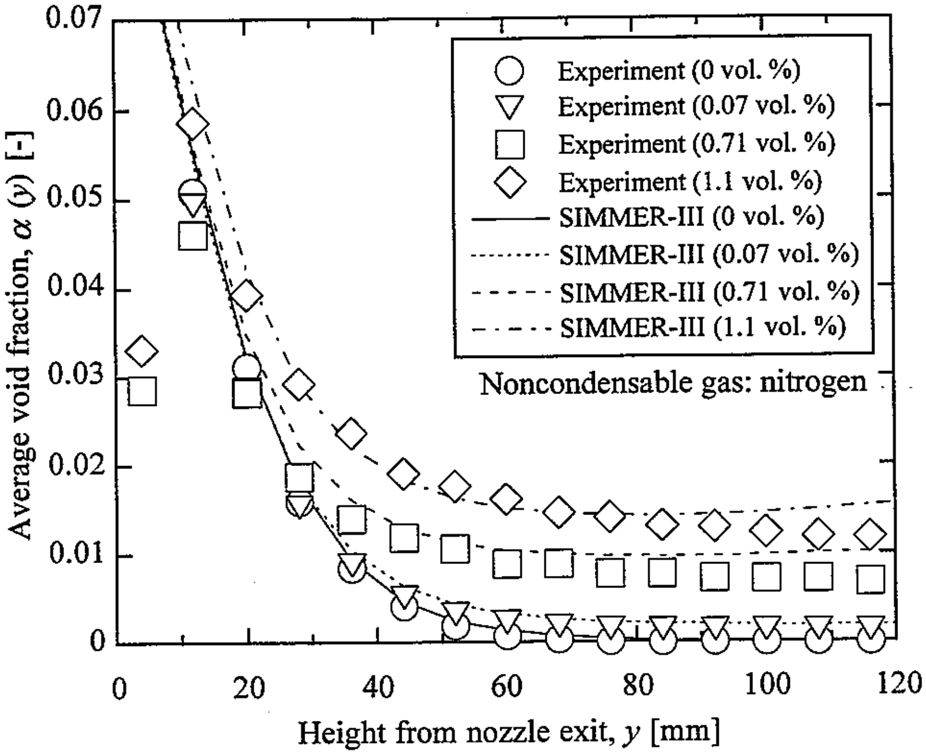

Fig. 19. Vertical distributions of void fractions for various nitrogen-concentrations.

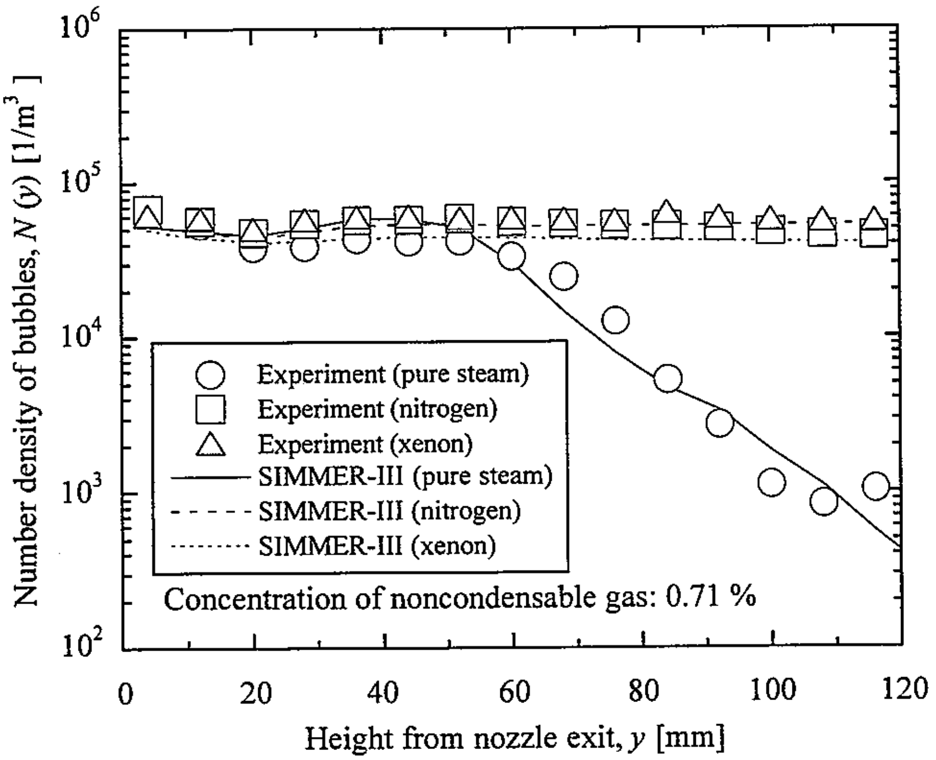

Fig. 20. Vertical distributions of number densities for different noncondensable gas.

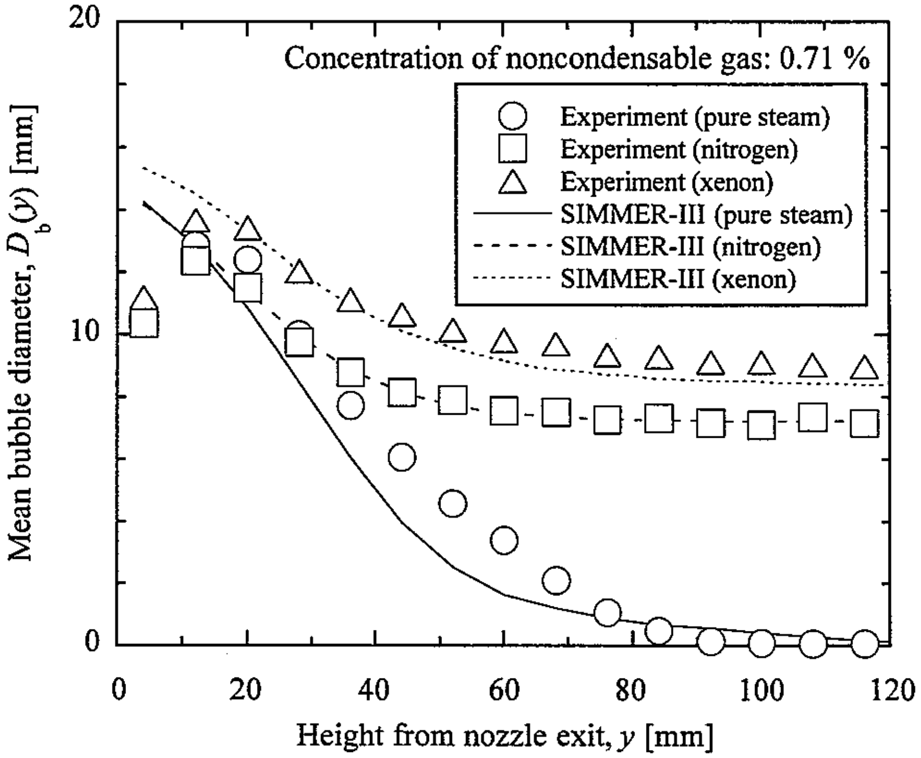

Fig. 21. Vertical distributions of bubble diameters for different noncondensable gas.

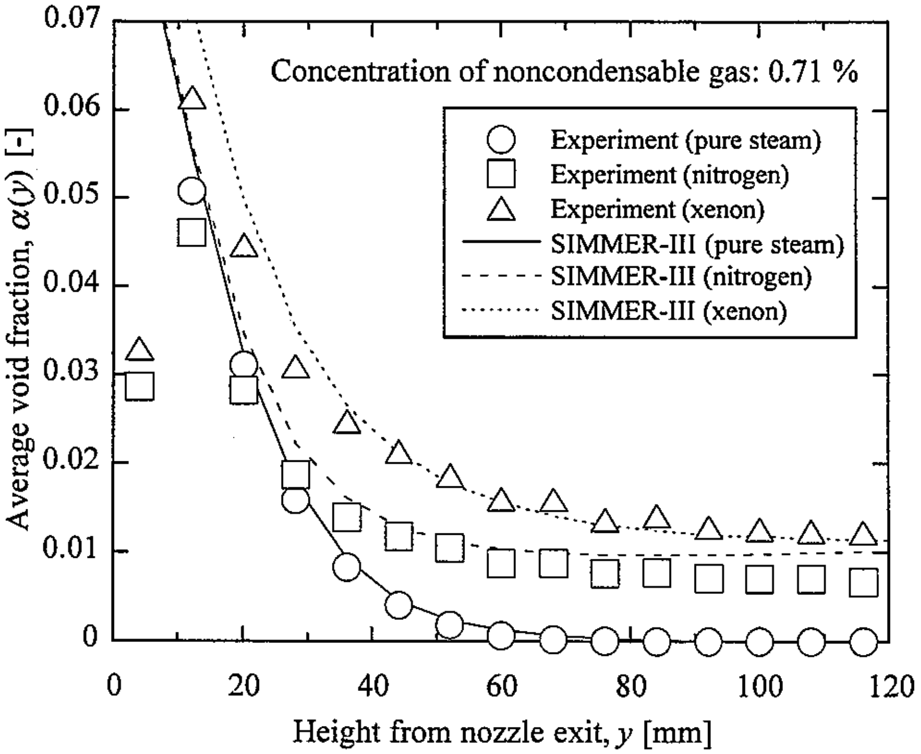

Fig. 22. Vertical distributions of void fractions for different noncondensable gas.

11 sec. (left-hand side)

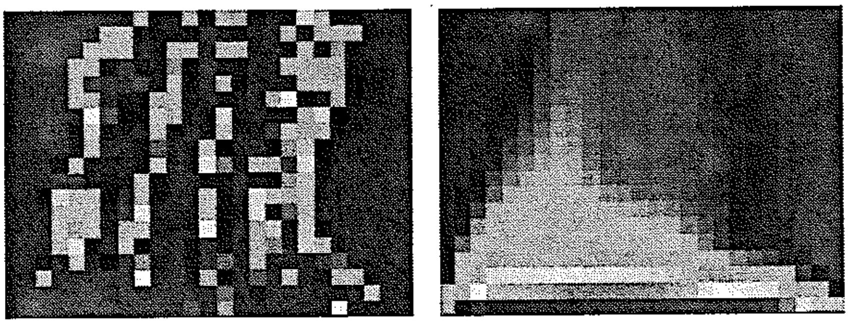

15 sec. (center)

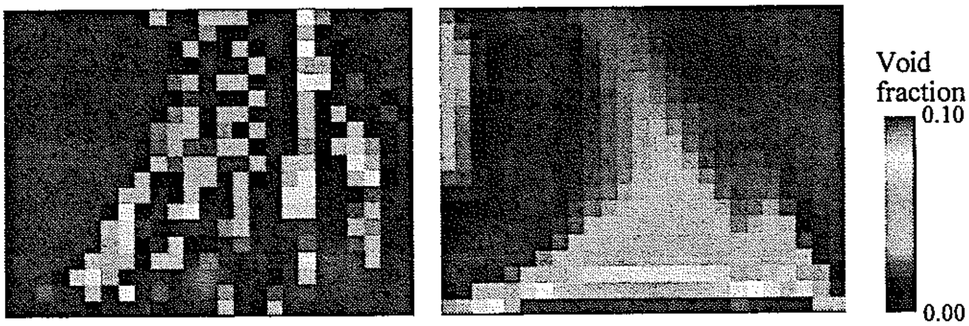

19 sec. (right-hand side)

(a) experiment (b) SIMMER-III

Fig. 23. Two-dimensional multi-bubble motion for steam-xenon system.

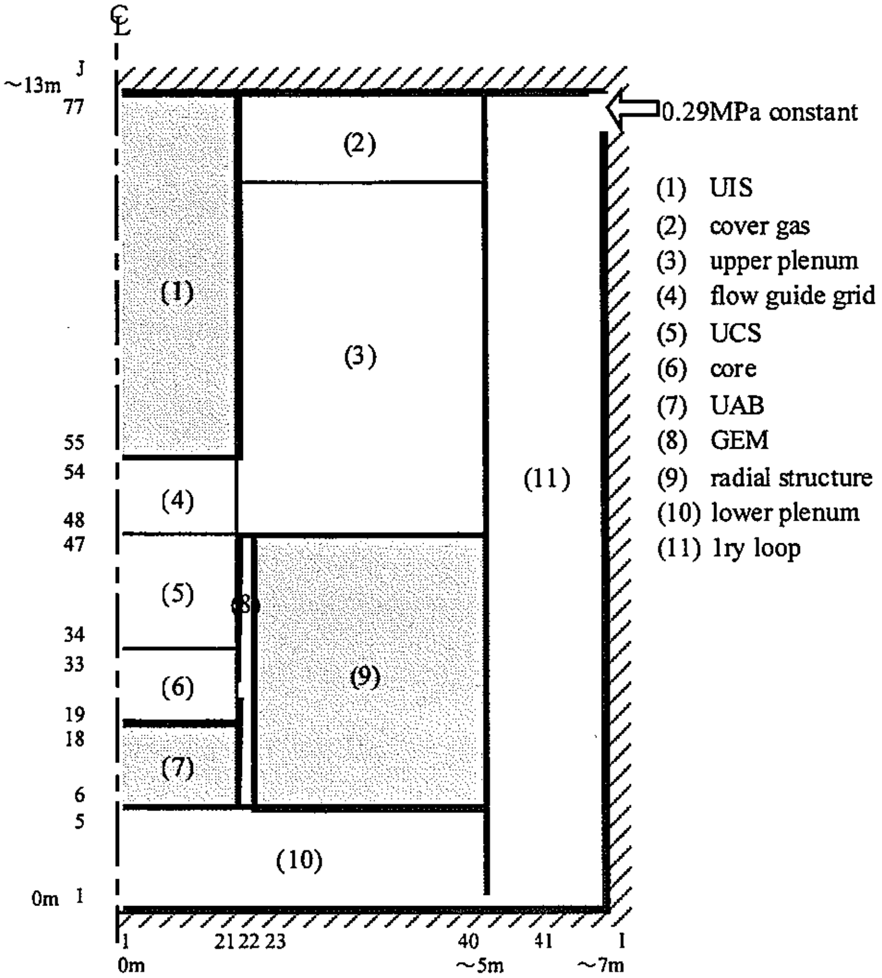

Fig. 24. Analystical system used in the analysis of PDE of typical FBR plant.

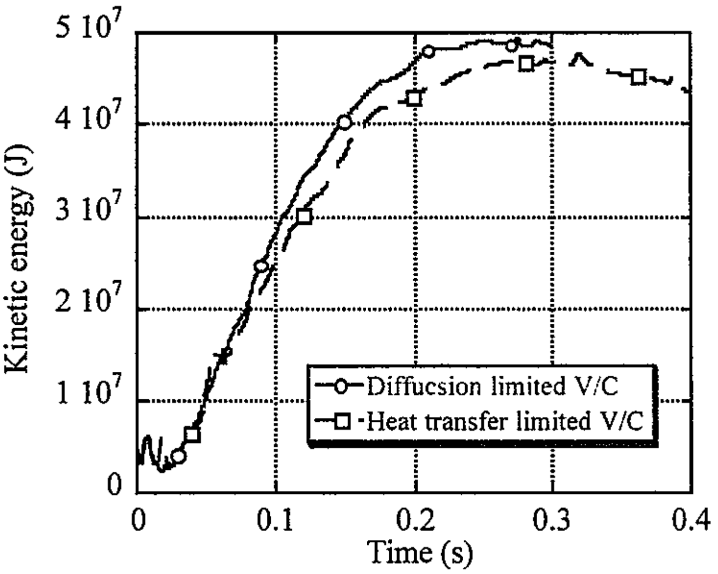

Fig. 25. Analystical system used in the analysis of PDE of typical FBR plant.

6. Conclusions

An advanced multicomponent V/C model has been developed to provide a generalized model for a fast reactor safety analysis code SIMMER-III. The model characterizes the V/C process associated with phase transition through heat-transfer and mass-diffusion limited models to follow the time evolution of the rector core under CDA conditions. By analyzing two series of multicomponent phase-transition experiments, the followings were demonstrated:

- SIMMER-III could predict approximate solutions of condensation behaviors in the mixture of vapor and noncondensable gas for variable amounts of and different species of noncondensable gas in the mixture.
- SIMMER-III could represent not only the behavior of multi-bubble condensation, but also the two-phase flow dynamics with the phase transition appropriately.

In addition, the application study to the PDE analysis indicates that the code could simulate the effects of multicomponent mixture on the phase transition practically. It can be expected that SIMMER-III using the present V/C model would describe the multicomponent phase-transition process reliably for core materials in sufficient physical details for use in the accident analysis of fast reactors.

Acknowledgments

The authors are grateful to Erhart A. Fischer of FZK for his significant contribution to forming the basis of the present study. Thanks are due to Kiyoshi Nakagawa, Takashi Uyama and Takashi Ishibashi of Kyushu University, and Masaaki Sugaya and Teppei Kondo of Nuclear Energy System Inc. for their contributions to this work. The present study has been performed as a joint research between JNC and Kyushu University.

Nomenclature

a	binary-contact area per unit volume (m^{-1})
$a_{\mathrm{A,B}}$	binary-contact area of the A/B interface per unit volume (m^{-1})
C_0	distribution parameter
c_{p}	specific heat at constant pressure ($J\ kg^{-1}\ K^{-1}$)
$D_{\mathrm{b}}(y)$	vertical distribution of mean bubble diameter (m)
D_{kg}	binary diffusivity of component k in a multicomponent mixture ($m^2\ s^{-1}$)
d	sphere diameter (m)
e	specific internal energy ($J\ kg^{-1}$)
G	volume flow rate of gas ($m^3\ s^{-1}$)
Gr	Grashof number
g	gravitational constant ($m\ s^{-2}$)
$\mathbf{g}$	gravitational acceleration ($m\ s^{-2}$)
h^*, h	heat-transfer coefficient with and without mass transfer, respectively ($W\ m^{-2}\ K^{-1}$)
$h_{\mathrm{A.B}}$	heat-transfer coefficient for side A of the A/B interface ($W\ m^{-2}\ K$)
i_{lg}	heat of vaporization ($J\ kg^{-1}$)
i	specific enthalpy ($J\ kg^{-1}$)
i_{Vap}	specific enthalpy of saturated (vaporization) vapor ($J\ kg^{-1}$)
i_{Con}	specific enthalpy of saturated (condensate) liquid ($J\ kg^{-1}$)
j_{g}	volumetric gas flux ($m\ s^{-1}$)
$K_{qq'}$	momentum exchange function between q and q' phases ($kg\ m^{-3}\ s^{-1}$)
k^*, k	mass-transfer coefficient with and without mass transfer, respectively ($kg\ m^{-2}\ s^{-1}$)
L	characteristic length (m) or cell size (m)
$N(y)$	vertical distribution of number density (m^{-3})
Nu	Nusselt number
N	number of condensable gases
$n(y)$	number distribution of bubbles
n_{nozzle}	number of nozzles
n_x	number of mesh cells in horizontal direction
p	pressure (Pa)
Pr	Prandtl number

q	heat-transfer rate per unit volume (W m^{-3})
$q^{\mathrm{I}}_{\mathrm{A,B}}$	net heat-transfer rate at the A/B interface per unit volume (W m^{-3})
R	correction factor for mass-transfer rate
Re	Reynolds number
Sc	Schmidt number
Sh	Sherwood number
T	temperature (K)
$T^{\mathrm{I}}_{\mathrm{A,B}}$	interface temperature at the A/B interface (W m^{-3})
T_{w}	surface temperature of sphere (K)
t	time (s)
V_{g}	velocity of gas (m s^{-1})
V_{gj}	drift velocity (m s^{-1})
VM	virtual mass term (kg m^{-2} s^{-2})
v	velocity (m s^{-1})
$\mathbf{v}$	velocity vector (m s^{-1})
W	molecular weight (kg mol^{-1})
x	mole fraction
y	coordinate normal to interface (m) or height from nozzle exit (m)

Greek letters

α	volume fraction
$\alpha(y)$	vertical distribution of void fraction
α_{p}	pool-average void fraction
α_{q}	volume fraction of q phase
$\Delta\rho$	density difference between gas and liquid (kg m^{-3})
Γ	mass-transfer rate per unit volume (kg s^{-1} m^{-3})
$\Gamma^{\mathrm{I}}_{\mathrm{A.B}}$	mass-transfer rate from component A to B (kg s^{-1} m^{-3})
μ	viscosity (Pa s)
κ	thermal conductivity (W m^{-1} K^{-1})
ρ	microscopic density (kg m^{-3})
$\overline{\rho}$	macroscopic (smeared) density (kg m^{-3}) ($=\alpha\rho$)
σ	surface tension (N m^{-1})

ω	mass fraction

Subscripts

A, B, C, D	species in multicomponent systems (A and B are used as condensable and noncondensable components, respectively)
f	liquid phase
G, g	vapor mixture
Gm	material component m in vapor field, representing fuel, steel, sodium and fission gas for m = 1 – 4, respectively.
i	interface quantity
K(k)	solid energy component contacting to fluid, representing L4, L5, L6, k1, k2 and k3 for k = 1 – 6, respectively.
k	species in multicomponent systems
km	energy component of structure surface, representing pin, left can wall and right can wall for m = 1 – 3, respectively.
Lm	energy component in liquid field, representing liquid fuel, liquid steel, liquid sodium, fuel particles, steel particles and control particles for m = 1 - 6, respectively.
M	mixture of components A and B
ng	noncondensable gas
o	condensation site
p	pool average
q	velocity field
Sat, sat	saturation
x	horizontal direction
y	vertical direction
z	normal direction
∞	bulk quantity

Superscripts

I(A/B)	interface identification of the A/B binary contact

References

[1] Bohl, W.R., Luck, L.B., 1990. SIMMER-II: A computer program for LMFBR disrupted core analysis, LA-11415-MS, Los Alamos National Laboratory.

[2] Smith, L.L., Bell, C.R., Bohl, W.R., Luck, L.B., Wehner, T.R., DeVault, G.P., Parker, F.R., 1985. The SIMMER program: Its accomplishment, Proc. Int. Mtg. on Fast Reactor Safety, pp. 977-980, Knoxville, TN, April 21-25.

[3] Kondo, Sa., Tobita, Y., Morita, K., Shirakawa, N., 1992. SIMMER-III: An advanced computer program for LMFBR severe accident analysis, Proc. Int. Conf. on Design and Safety of Advanced Nuclear Power Plant (ANP '92), Vol. IV, pp. 40.5-1-40.5-11, Tokyo, Japan, October 25-29.

[4] Tobita, Y., Kondo, Sa., Yamano, H., Fujita, S., Morita, K., Maschek, W., Louvet, J., Coste, P., Pigny, S., 2000. Current status and application of SIMMER-III, An advanced computer program for LMFR Safety Analysis, Proc. 2nd. Japan-Korea Symposium on Nuclear Thermal Hydraulics and Safety (NTHAS-2), Fukuoka, Japan, October 15-18.

[5] Kondo, Sa., Brear, D.J., Tobita, Y., Morita, K., Maschek, W., Coste, P., Wilhelm, D., 1997. Status and achievement of assessment program for SIMMER-III, A multiphase, multicomponent code for LMFR safety analysis, Proc. 8th. Int. Topical Mtg. on Nuclear Reactor Thermal-Hydraulics (NURETH-8), Vol. 3, pp. 1340-1348, Kyoto, Japan, September 30-October 3.

[6] Kondo, Sa., Tobita, Y., Morita, K., Brear, D.J., Kamiyama, K., Yamano, H., Fujita, S., Maschek, W., Fischer, E.A., Kiefhaber, E., Buckel, G., Hesserschwerdt, E., Coste, P., Pigny, S., 1999. Current status and validation of the SIMMER-III LMFR safety analysis code, Proc. 7th. Int. Conf. on Nuclear Engineering (ICONE-7), No. 7249, Tokyo, Japan, April 19-23.

[7] Boulanger, F., Coste, P., 1997. LMFR accidents: verification of the SIMMER-III code for the expansion phase, Proc. 8th. Int. Topical Mtg. on Nuclear Reactor Thermal-Hydraulics (NURETH-8), Vol. 3, pp. 1349-1356, Kyoto, Japan, September 30-October 3.

[8] Tobita, Y., Morita, K., Kawada, K., Niwa, H., Nonaka, N., 1999. Evaluation of CDA Energetics in the Prototype LMFBR with Latest Knowledge and Tools, Proc. 7th. Int. Conf. on Nuclear Engineering (ICONE-7), No. 7145, Kyoto, Japan, April 19-23.

[9] Morita, K., Rineiski, A., Kiefhaber, E., Maschek; W., Flad, M., Rimpault, G., Coste, P., Pigny, S., Kondo, Sa., Tobita, Y., Fujita, S., 2001. Mechanistic SIMMER-III analyses of severe transients in accelerator driven systems (ADS), Proc. 9th. Int. Conf. on Nuclear Engineering (ICONE-9), No. 150, Nice, France, April 8-12.

[10] Morita, K., Kondo, Sa., Tobita, Y., Brear, D.J., 1999. SIMMER-III applications to fuel-coolant interactions, Nucl. Eng. and Des., 189, 337-357.

[11] Bohl, W.R., Berthier, J., Goutagny, Schmuck, P., 1990. AFDM: An advanced fluid-dynamics model, Volume IV: The AFDM heat- and mass-transfer solution algorithm, LA-11692-MS, Vol. IV, Los Alamos National Laboratory.

[12] Bohl, W.R., Wilhelm, D., Parker, F.R., Berthier, J., Goutagny, L., Ninokata, H., 1990b.

AFDM: An advanced fluid-dynamics model, Volume I: Scope, approach, and summary, LA-11692-MS, Vol. I, Los Alamos National Laboratory.

[13] Tobita, Y., Morita, K., Kondo, Sa., Shirakawa, N., Bohl, W.R., Parker, F.R., Brear, D.J., 1991. Interfacial area modeling for a multiphase, multicomponent fluid-dynamics code, Proc. Int. Conf. on Multiphase Flows '91-TSUKUBA, Vol. 2, pp. 361-364, Tsukuba, Japan, September 24-27.

[14] Morita, K., Fischer, E.A., 1998. Thermodynamic properties and equations of state for fast reactor safety analysis, Part I: Analytic equation-of-state model, Nucl. Eng. and Des., 183, 177-191.

[15] Morita, K., Fischer, E.A., Thurnay K., 1998. Thermodynamic properties and equations of state for fast reactor safety analysis, Part II: Properties of fast reactor materials, Nucl. Eng. and Des., 183, 193-211.

[16] Bohl, W.R, 1986. Investigation of steam explosion loadings using SIMMER-II, NUREG-CP-72, Vol. 6, pp. 159-174, U.S. Department of Energy.

[17] Ghiaasiaan, S.M., Kamboj, B.K., Abdel-Khalik, S.I., 1995. Two-fluid modeling of condensation in the presence of noncondensables in two-phase channel flows, Nucl. Sci. Eng., 119, 1-17.

[18] Yao, G.F., Ghiaasiaan, S.M., Eghbali, D.A., 1996. Semi-implicit modeling of condensation in the presence of non-condensables in the RELAP5/MOD3 computer code, Nucl. Eng. and Des., 166, 217-291.

[19] Yao, G.F., Ghiaasiaan, S.M., 1996. Numerical modeling of condensing two-phase flows, Numerical Heat Transf., B, 30, 137-159.

[20] Bird, B., Stewart, W.E., Lightfoot, E.N., 1960. Transport Phenomena, John Wiley and Sons, New York.

[21] Morita, K., Tobita, Y., Kondo, Sa., Fischer, E.A., 1999. SIMMER-III analytic thermophysical property model, JNC TN9400 2000-004, Japan Nuclear Cycle Development Institute.

[22] Jackson, J.F., 1978. Nuclear reactor safety, quarterly progress report, October 1-December 31, 1977, LA-7195-PR, Los Alamos Scientific Laboratory.

[23] Jackson, J.F., 1978. Nuclear reactor safety, quarterly progress report, January 1-March 31, 1978, LA-7278-PR, Los Alamos Scientific Laboratory.

[24] Dhir, V.K., 1971. Quasi-steady laminar film condensation of steam on copper sphere, J. Heat Transfer, 347-351.

[25] Dhir, V.K., Lienhard, J., 1971. Laminar film condensation on plane and axisymmetric bodies in nonuniform gravity, J. Heat Transfer, 97-100.

[26] Peterson, P.F., 1996. Theoretical basis for the Uchida correlation for condensation in reactor containments, Nucl. Eng. and Des., 162, 301-306.

[27] Herranz, L.E., Anderson, H.A., Corradini, M.L., 1998. A diffusion layer model for steam condensation within the AP600 containment, Nucl. Eng. and Des., 183, 133-150.

[28] Ishii, M. and Zuber, N., 1979. Drag coefficient and relative velocity in bubbly, droplet or particulate flow, AIChE J., Vol. 25, pp. 843-855.

[29] Ishii, M. and Chawla, T.C., 1979. Local drag lows in dispersed two-phase flow, ANL-79-105, Argonne National Laboratory.

[30] Suzuki, T., Tobita, Y., Yamano, H. and Kondo, Sa., 2000. SIMMER-III analysis of gas-liquid flows with large liquid densities, Proc. 2nd Japan-Korea Symposium on Nuclear Thermal Hydraulics and Safety (NTHAS-2), pp. 73-80, Fukuoka, Japan, October 15-18.

[31] Morita, K., Tobita, Y., Kondo, Sa. and Nonaka, N., 1997. SIMMER-III applications to key phenomena of CDAs in LMFR," Proc. 8th Int. Topical Mtg on Nuclear Reactor Thermal-Hydraulics (NURETH-8), Vol. 3, pp. 1332-1339, Kyoto, Japan, September 30-October 3.

[32] Kondo, Sa., Yamano, H., Suzuki, T., Tobita, Y., Fujita, S., Cao, X., Kamiyama, K., Motita, K., Fischer, E.A., Brear, D.J., Shirakawa, N., Mizuno, M., Hosono, S., Kondo, T., Maschek, W., Kiefhaber, E., Buckel, G., Rineinski, A., Flad, M., Coste, P., Pigny, S., Louvet, J. and Cadiou, T., 2000. SIMMER-III: A computer program for LMFR core disruptive accident analysis, JNC TN9400 2001-002, Japan Nuclear Cycle Development Institute.